



**HAL**  
open science

# A roadmap to high-resolution standard microcoil MAS NMR spectroscopy for metabolomics

Alan Wong

► **To cite this version:**

Alan Wong. A roadmap to high-resolution standard microcoil MAS NMR spectroscopy for metabolomics. *NMR in Biomedicine*, 2022, pp.e4683. 10.1002/nbm.4683 . cea-03509128

**HAL Id: cea-03509128**

**<https://cea.hal.science/cea-03509128>**

Submitted on 4 Jan 2022

**HAL** is a multi-disciplinary open access archive for the deposit and dissemination of scientific research documents, whether they are published or not. The documents may come from teaching and research institutions in France or abroad, or from public or private research centers.

L'archive ouverte pluridisciplinaire **HAL**, est destinée au dépôt et à la diffusion de documents scientifiques de niveau recherche, publiés ou non, émanant des établissements d'enseignement et de recherche français ou étrangers, des laboratoires publics ou privés.

1  
2  
3  
4  
5  
6  
7  
8  
9  
10  
11  
12  
13  
14  
15  
16  
17  
18  
19

**A roadmap to high-resolution standard microcoil MAS NMR spectroscopy  
for metabolomics**

Alan Wong

NIMBE, CEA, CNRS, Université Paris-Saclay, CEA Saclay, 91191 Gif-sur-Yvette, France;

corresponding author: [alan.wong@cea.fr](mailto:alan.wong@cea.fr), +33 (0) 1 48 25 40 54

Word count: 8727

## 20 **Abstract**

21 The current microcoil probe technology has emerged as a significant advancement in NMR  
22 applications to biological research of biofluids and continued to excel as a hyphenated tool  
23 with other prominent microdevices opening many new possibilities in multiple omics fields.  
24 However, this is contrary to biological samples like intact tissue or organism. This is due to  
25 the considerable challenges of incorporating the microcoil in a magic-angle spinning (MAS)  
26 probe without relinquishing the acquisition of high-resolution spectral data. Not until 2012, a  
27 microcoil MAS probe had shown promises on profiling the metabolome in submilligram  
28 tissue biopsy with spectral resolution *on par* with the conventional high-resolution MAS  
29 (HR-MAS) NMR. This result had subsequently triggered a great interest in the possibility of  
30 NMR analysis with microgram tissues and strived toward the probe development of 'high-  
31 resolution' capable microcoil MAS NMR spectroscopy. This review gives an overview of the  
32 issues and challenges in the probe development and summarizes the advancements toward  
33 metabolomics.

34

35 Keywords: microcoil; magic-angle spinning; high-resolution; sensitivity; metabolomics;

36

## 37 **Selected Abbreviations**

38

39	$\chi$	magnetic susceptibility factor
40	$\mu$	micro
41	$B$	magnetic field
42	$B_0$	external applied magnetic field
43	$B_1$	transverse radiofrequency magnetic field
44	$B_z$	dipole field of a magnetic moment
45	DNP	dynamic nuclear polarization
46	FWHM	full-width at half-maximum
47	$i$	electrical current
48	HMQC	heteronuclear multiple quantum coherence
49	HR-MAS	high-resolution magic-angle spinning
50	rf	radiofrequency
51	SNR	signal-to-noise ratio

52

## 53 **Introduction**

54 Metabolomics is a significant omics field that studies the chemical fingerprints of small  
55 molecule metabolites that responds to specific cellular processes. It plays a vital role in  
56 untangling many complexities in life science. This is thanks to the vast advancement in  
57 bioanalytical technology. *Ex vivo* NMR spectroscopy has found tremendous success due to its  
58 simplicity and versatility in acquiring unbiased and rich metabolic information on diverse  
59 biospecimens from biofluids to biotissues. In particular, High-Resolution Magic-Angle  
60 Spinning (HR-MAS) – rapid sample spinning under a magnetic field – is an indispensable  
61 technique in NMR studies of animal and human tissue.<sup>1-7</sup> This is attributed to its ability to  
62 acquire superior spectral resolution data from heterogeneous specimens (*i.e.*, *on par* with the  
63 liquid state NMR). However, despite its significant applications to NMR-based  
64 metabolomics, the probe technology of HR-MAS has remained nearly the same in the past  
65 decades. The latest substantial advancement would be the fully automated HR-MAS probe  
66 (iProbe™) in 2018.<sup>8</sup> In contrast, other bioanalytical technologies like mass spectrometry  
67 (MS),<sup>9</sup> magnetic resonance imaging,<sup>10</sup> and positron emission tomography<sup>11</sup> continue  
68 advancing. There is a common conception that the current number of MS-based metabolomic  
69 studies has overtaken NMR.<sup>12</sup> A literature search in Web of Science™ shows a nearly 2:1  
70 ratio between MS and NMR metabolomics. Therefore, for NMR spectroscopy to continue to  
71 be a frontline *ex vivo* analytic platform, new technologies and concepts should be explored  
72 entirely to address the limitations.

73

74 Presently, there is a general tendency to develop biotechnology toward microscopic  
75 specimens. The notion is to advance the underlining omics understanding at a single-cell (or  
76 even subcellular) level.<sup>13</sup> One weakness in NMR spectroscopy is the inherent low detection  
77 sensitivity. The HR-MAS application generally requires 5–10 mg samples to compensate for  
78 the low sensitivity. This hinders the possibility of analyzing  $\mu\text{g}$  samples. Indeed, using a high  
79 magnetic field is an approach to enhance detection sensitivity. However, the running cost is  
80 exponential with the field. A cost-effective method is to utilize a miniature radiofrequency  
81 (rf) coil, so-called microcoil ( $\mu\text{coil}$ ), for optimizing the sample and coil volume ratio (*i.e.*,  
82 filling factor). The prime concern is maintaining high spectral resolution data to allow in-  
83 depth metabolic profiling. This is achieved in liquid-state NMR by surrounding the microcoil  
84 with magnetic susceptibility-matched material to facilitate the field shimming<sup>14</sup> or using a

85 zero-susceptibility  $\mu$ coil.<sup>15</sup> These adaptations have subsequently led to significant  
86 advancements in microcoil applications to biofluid studies.<sup>16</sup>

87

88 The fact that nano-scale volume of tissue and cell can be optimally detected and analyzed  
89 with a cost-effective approach makes  $\mu$ coil an appealing technology. However, the  $\mu$ coil  
90 technology under MAS, or microcoil MAS, is lagging. This is due to the challenges of  
91 implementing a stable  $\mu$ coil that can endure a rapid sample spinning. The early designs  
92 centered on implanting an independent microcoil onto a conventional MAS probe and  
93 utilizing the existing stator to propel the sample spinning. The first microcoil under MAS was  
94 introduced in 2006 with a piggyback design<sup>17</sup> and was shortly followed by an inductive  
95 spinning  $\mu$ coil approach.<sup>18</sup> These results had subsequently sparked the interest in the  
96 commercial and academic groups and have resulted in multiple commercial probes with rotor  
97 diameters ranging from 1-mm down to 0.5-mm.<sup>19-21</sup> These state-of-the-art probes are  
98 explicitly designed to spin mg-scale samples up to 100+ kHz to narrow the resonance  
99 linewidth that arises from the nuclear spin networks. As a result, they have an immediate  
100 impact on the MAS applications in many research fields of biosolids,<sup>22-28</sup> including the study  
101 of membrane proteins<sup>29</sup> and amyloid fibers.<sup>30</sup> However, the ultra-fast sample spinning is not  
102 of concern in the metabolomic study of delicate samples like tissues and cells. It is considered  
103 an unfavorable condition because of the enormous centrifugal force exerted on the sample. A  
104 significant concern in designing a microcoil probe for metabolomics is its ability to acquire  
105 sufficient spectral resolution data to unfold the dense metabolic <sup>1</sup>H resonance pattern and  
106 permit thorough peak analyses for identification and quantification. Moreover, the ability to  
107 acquire reproducible data is also a crucial factor. This depends on the stability of the probe  
108 and the consistency of the sample preparation for the NMR measurements.

109

110 The possibility of <sup>1</sup>H NMR profiling  $\mu$ g biopsy tissue under MAS condition was first  
111 evaluated in 2012.<sup>31</sup> It subsequently triggered the interest of striving for the possibility of  
112 'high-resolution' standard microcoil MAS toward NMR-based metabolomics. Despite the vast  
113 number of excellent review literature on HR-MAS NMR spectroscopy,<sup>1-3</sup> microcoil NMR,<sup>16</sup>  
114 and microcoil MAS,<sup>22-30</sup> there are none on the 'high-resolution' standard microcoil MAS.  
115 Hence, this review aims to bridge the high-resolution microcoil technology under MAS  
116 conditions with metabolomics and provides the fundamental basis for future advancements. It

117 summarizes the current developments, emphasizing our efforts from a nonexistence state to a  
 118 beacon of possibility.

119

## 120 **NMR considerations**

121 NMR is a spectroscopic technique that characterizes the net magnetization  $\mathbf{M}$  induced in a  
 122 sample exposed to an external field  $\mathbf{H}_0$ , which can be described by a magnetic susceptibility  
 123 factor  $\chi$ ,  $\mathbf{M} = \chi\mathbf{H}_0$ . The net magnetic field  $\mathbf{B}_0$  in a sample exposed to  $\mathbf{H}_0$  can be expressed as

$$124 \quad \mathbf{B}_0 = \mu_0(\mathbf{H}_0 + \mathbf{M}) = \mu_0\mu\mathbf{H}_0 \quad (1)$$

125 where  $\mu_0$  is a permeability of free space, and  $\mu = 1 + \chi$  is the permeability of the sample.  $\chi$   
 126 is a dimensionless quantity that indicates the extent of the magnetization  $\mathbf{M}$  in a sample under  
 127 an external field. Several sources contribute to  $\mathbf{M}$ , which arise from the energy current within  
 128 atoms, electrons, and nucleons. They are essentially responsible for an NMR resonance line  
 129 intensity and shape. This review focuses only on the magnetizations that contribute to the  
 130 resonance intensity and resolution. Note that in NMR and MRI, the external magnetic field is  
 131 often denoted as  $B_0$  rather than  $H_0$ ; thereby,  $B_0$  will be used hereafter.

132

133 **Sensitivity.** It is a hallmark problem for NMR and is attributed to the nuclear spin  
 134 magnetization  $M_0$ . At thermal equilibrium,  $M_0$  can be expressed by the Boltzmann  
 135 distribution, for 1/2-spin nuclei,

$$136 \quad M_0 = \frac{\gamma\hbar N}{2} P, \text{ where } P = \frac{N_\alpha - N_\beta}{N} \equiv \tanh\left(\frac{\gamma\hbar B_0}{2k_B T_s}\right) \quad (2)$$

137 where  $\gamma$  is the gyromagnetic ratio,  $\hbar$  ( $h/2\pi$ ) is the Plank's constant,  $N$  is the total number of  
 138 spins ( $N_\alpha + N_\beta$ ), and  $P$  is the nuclear polarization,  $B_0$  is the applied external magnetic field,  $k_B$   
 139 and  $T_s$  is the Boltzmann's constant and the sample temperature. The intensity of a detected  
 140 signal is proportional to the polarization. For example, at a typical NMR field of 11.7 T at an  
 141 ambient temperature of 300 K, only about 40 ppm of protons are polarized. Such small  
 142 polarization is the very reason for the inherently low detection sensitivity in NMR.

143

144 Aside from  $M_0$ , the signal intensity – quantified by a signal-to-noise ratio (SNR) – also  
 145 depends on the instrumentations, which can be breakdown into a few distinct components:<sup>32</sup>

$$146 \quad SNR \propto [\gamma B_0]_{\substack{\text{oscillation} \\ \text{frequency}}} \times [M_0]_{\text{magnetization}} \times [B_1/i]_{\substack{\text{coil} \\ \text{efficiency}}} \times \left[\frac{1}{\sqrt{T_c R_c}}\right]_{\substack{\text{thermal} \\ \text{noise}}} \quad (3)$$

147 The first two correspond to the oscillation and the polarized magnetization of the nuclear  
 148 spin. The  $B_1/i$  term is defined as the transverse magnetic field  $B_1$  per unit current associated

149 with the rf efficiency inside the coil volume. The last term is the thermal noise ascribed from  
150 the coil's temperature  $T_c$  and resistance  $R_c$ . Essentially, the strategy for increasing the SNR is  
151 by manipulating the individual components through physics and engineering. For example, a  
152 common conception is to raise the external magnetic field  $B_0$  to enhance the spin oscillation  
153 and magnetization. Since the signal and noise increase as a square and a square root of  
154 the  $B_0$  field, therefore the overall SNR increases as  $B_0^{3/2}$ . The current highest commercial  
155 NMR field is 28 T (1.2 GHz for  $^1\text{H}$ ).<sup>33</sup> Further increases are expected to be challenging and  
156 expensive to overcome the issues of field homogeneity and stability.

157

158 Other approaches include manipulating the spin magnetization  $M_0$  by polarization transfer. It  
159 involves transferring the polarization from nuclei with high magnetic moment to lower  
160 magnetic moment nuclei, offering a gain in sensitivity corresponding to the ratio of their  
161 gyromagnetic ratios,  $\gamma_{\text{high}}/\gamma_{\text{lower}}$ . This is routinely applied in solid-state  $^{13}\text{C}$  (or  $^{29}\text{Si}$ ) NMR  
162 pulse experiments by polarizing the  $^{13}\text{C}$  spins with the neighboring  $^1\text{H}$  and can gain up to a  
163 factor of  $\sim 4$  ( $\gamma_{^1\text{H}}/\gamma_{^{13}\text{C}}$ ). Similarly, the polarization transfer from the electron spin to nuclear  
164 spin can have a tremendous gain (up to  $10^4$ – $10^5$ ) because of the large Zeeman splitting in the  
165 electron spin. Such transfer enters the regime of hyperpolarization, where the spin  
166 polarization deviates from thermal equilibrium. This phenomenon between the electron and  
167 nuclear is known as Dynamic Nuclear Polarization (DNP). Academic and commercial  
168 researchers have invested tremendous efforts in integrating DNP with high-field NMR and  
169 MRI research.<sup>34–36</sup> In liquids, dissolution-DNP has already been widely integrated with  
170 advanced spectroscopy and imaging experiments and has opened many new opportunities  
171 including *in vivo* applications.<sup>34</sup>

172

173 Other hyperpolarization schemes have also been considered and applied. For example, a brute  
174 force approach would be lowering the sample temperature to millikelvin in high magnetic  
175 fields.<sup>37</sup> This is, of course, not feasible for biological samples like tissues and organisms.

176 Other schemes have found success in the bioapplications; these include optical pumping with  
177 noble gases ( $^{129}\text{Xe}$ ) for sensing the biomolecule activities,<sup>38</sup> photochemically-induced DNP  
178 (photo-CIDNP) for investigating protein folding and biomolecular interactions,<sup>39</sup> and  
179 parahydrogen-induced-polarization (PHIP) for kinetic studies.<sup>40</sup> A common characteristic of  
180 these schemes is the inclusion of chemical additives or so-called polarizing agents.

181

182 An approach to gain SNR without polarizing agents is by reducing the electronic thermal  
183 noise with a cryogenically cooled rf detection coil. It requires a specific probe design,  
184 denoted as cryoprobe, allowing to reduce the operating temperature of the coil to around 20 K  
185 while keeping the sample at an ambient temperature. Cryoprobes have become routinely  
186 employed in liquid-state NMR application to biomolecular research.<sup>41</sup> The coil is constructed  
187 with a superconducting wire, such as  $\text{YBa}_2\text{Cu}_3\text{O}_{7-d}$  (YBCO), with zero resistance under 20–  
188 30 K, reducing the electronic noise and can lead to an SNR gain up to 4–5 folds. The use of a  
189 cold coil is of particular interest in the microcoil probe because of the increased noise level as  
190 the coil size decreases; therefore, it is logical to integrate the cryoprobe technology with the  
191 microcoil. Brey and his team<sup>42</sup> have designed and constructed a high-resolution capable  
192 cryoprobe with a 1-mm coil for liquid-state NMR spectroscopy. The probe has an active  
193 sampling volume of 6.3  $\mu\text{L}$  with superconducting YBCO coils cooled to about 20 K. The  
194 resultant mass sensitivity (SNR per unit mass) is more than 20 times higher than a standard 5-  
195 mm probe. One of the engineering challenges in cryoprobe is implanting a sharp thermal  
196 gradient of a vacuum barrier between the confined space of the cold coil and the ambient  
197 sample without relinquishing the filling factor. This indeed has dramatically hindered the  
198 development of cryoprobes under MAS conditions. The first probe, so-called cyrocoil MAS,  
199 was introduced in 2008 designed and constructed by Mizuno with his team at JEOL,<sup>43</sup> but  
200 only recently, a more accessible probe was released by Bruker (BioSolids CryoProbe™) and  
201 has found succussed in the biosolids.<sup>44</sup> The notion of 'high-resolution' spectroscopy would  
202 hugely complicate the design and construction of a cyrocoil 'HR'-MAS probe. To this day,  
203 only one attempt has been made by Doty and his team.<sup>45</sup>

204

205 As these enhancement schemes require substantial instrumentation and operation costs, it is  
206 of interest to explore cost-effective alternatives. One approach is optimizing the technology  
207 in the rf coil efficiency, the  $B_1/i$  term in Equation 3, by using rf microcoils.

208

209 **Radiofrequency microcoil.** Electronically, the rf coil – the closest probe component to the  
210 sample – functions as an inductive antenna that receives the voltage-induced rf transmitting  
211 by the precession of the spin magnetization of the sample. The transverse rf magnetic field  
212 efficiency,  $B_1/i$ , of an rf coil plays a role in SNR and has been discussed in detail by Hoult  
213 and Richards,<sup>32</sup> and reviewed by Webb.<sup>46</sup> It implies that the SNR is inversely proportional to  
214 the diameter of the saddle and solenoid coil; thus, the gain in sensitivity can be achieved by

215 miniaturizing the coil around the small sample volume. Herein, we will focus on the solenoid  
216 coil. It has a cylindrical geometry by winding a long wire with multiple helical turns  
217 producing an effectively strong and uniform transverse field inside the cylindrical volume.  
218 The  $B_1/i$  term in Equation 3 can be expressed using Biot-Savart law,

$$219 \quad \frac{B_1}{i} = \frac{n\mu_0}{2r} \frac{1}{\sqrt{1+(l/2r)^2}} \quad (4)$$

220 where  $n$  is the number of helical turns,  $r$  and  $l$  are the radius and length of the solenoid coil,  
221 and  $\mu_0$  is the permeability of the vacuum. Evidently, with a fixed  $l/2r$  factor,  $B_1/i$  increases  
222 with the inverse of the coil diameter. Minard and Wind have outlined a didactic guideline for  
223 designing  $\mu$ -size solenoids ( $2r \leq 1$ -mm) with optimal rf performance.<sup>47,48</sup> Sweedler and Webb  
224 and their team have exploited the simplicity of the solenoid design and demonstrated the  
225 possibility of acquiring high-quality  $^1\text{H}$  NMR signals of nano-volume samples with coils less  
226 than 1-mm in diameter.<sup>14,49</sup> This result has set off a substantial interest in academic and  
227 commercial research on microcoil probe technology and made significant advancements in  
228 studying volume/mass limited samples. There are several review literature on microcoil NMR  
229 spectroscopy.<sup>46,50-56</sup> Indeed, the capability of analyzing small volumes makes it a natural  
230 choice for coupling with chemical microseparation techniques<sup>57</sup> and with microfluidics. The  
231 latter includes an innovative hand-held NMR unit, referred to as diagnostic magnetic  
232 resonance (DMR), developed by Weissleder and his team.<sup>58</sup> It integrates a microcoil with a  
233 microfluidic system to rapidly screen biospecimens such as bacteria and tumor cells by  
234 discriminating their transverse relaxation rates. This technique has recently advanced in  
235 conjunction with DNP, denoted as hyperpolarized micromagnetic resonance spectrometer  
236 (HMRS).<sup>59</sup> It permits an ultra-high sensitivity detection for a real-time NMR analysis of the  
237 metabolic flux in living cells. The possibility of noninvasive monitoring with HMRS of  
238 tumor progression and treatment efficacy had been proposed to be tested in clinical trials.<sup>59</sup> In  
239 the commercial sectors, they have adapted a balance between sensitivity and sampling  
240 volume for a routine-based biomolecular study. For example, Bruker has incorporated a 1-  
241 mm diameter coil with an active sampling volume of about 2.5  $\mu\text{L}$ .<sup>60</sup>

242  
243 Although the microcoil technology is well adapted in the NMR studies of biofluids and has  
244 continued to advance in novel applications, it is entirely different for samples under MAS (or  
245 microcoil MAS). This is due to the engineering challenges of implementing a microcoil  
246 inside a MAS stator that can endure a rapid sample spinning. The early developments (with  
247 coil diameter  $\leq 1$ ) are explicitly targeted on solid-state experiments. This is because of the

248 considerable advantage of fast sample spinning experiments with small rotors and the  
249 strong  $B_1$  field strength from the small coil. The first successful experiment was carried out in  
250 2006 by Kentgens and his team using a so-called piggyback design.<sup>17</sup> To overcome the  
251 challenge of implementing a microcoil, a standard 4-mm stator was used to spin a standard  
252 rotor piggybacking an  $\mu$ -size sampling capillary centered inside a microcoil coil cavity. This  
253 clever design permits a stable spinning of the sampling capillary driven by the conventional  
254 stator while enhancing the signal with a microcoil. The results had demonstrated the  
255 possibility of acquiring isotropic spectra on  $\mu$ g of solids and the  $B_1$  efficiency of producing a  
256 strong decoupling  $B_1$  field for line narrowing experiments.

257

258 In 2012, JEOL introduced the first commercial microcoil MAS probe with a 0.75-mm  
259 stator,<sup>19</sup> and shortly followed by Bruker countering with a 0.7-mm probe.<sup>20</sup> These probes are  
260 capable of sample spinning as high as 110 kHz, offering the possibility of suppressing the  
261 large nuclear spin magnetizations ascribed from the spin-interactions to yield narrow NMR  
262 lines for characterizing solids. Hence, these microcoil MAS probes are also known as  
263 ultrafast MAS. Recently, a research team has introduced a 0.5-mm MAS probe that offers a  
264 groundbreaking sample spinning at 170 kHz.<sup>21</sup> These commercial ultrafast probes have now  
265 widened the NMR applications on biosolids, including  $^1\text{H}$  NMR,<sup>22-30</sup> an area that was first  
266 considered impossible because of the intrinsically broad  $^1\text{H}$  signals in biosolids.

267

268 The extensive developmental works in the ultrafast MAS probe have been primarily focused  
269 on increasing the sample spinning and the rf field efficiency and reducing the sample heating  
270 ascribed to the rotor friction and rf. There is little attention on the line broadening caused by  
271 the static probe materials, which sample rotation cannot suppress. Consequently, the optimal  
272 line resolution from these probes is insufficient for  $^1\text{H}$  metabolic investigation on samples  
273 like tissue biopsy. Most ultrafast MAS probes offer 0.01–0.02 ppm linewidth at best and  
274 often with a distorted lineshape that field shimming cannot correct.

275

276 **Line resolution.** To comprehend the source of the line-width and -shape of an NMR  
277 resonance, one must understand the origins of the effective field  $\mathbf{B}$  experienced by the sample  
278 (Equation 1), which depends on the susceptibility factor  $\chi$  arising from the local dipole  
279 magnetic moment  $m$ . For example, when a metabolite is immersed in an isotropic solution, its  
280 susceptibility induces an additional field upon the metabolite and results in a resonance shift.

281 However, metabolites in a complex biological medium are usually distributed in different  
 282 cellular compartments and morphologies, each with a different susceptibility field.  
 283 Consequently, this creates a heterogenous field for the metabolic protons to resonate at a  
 284 series of varying resonance shifts resulting in line broadening. In NMR, this is known as  
 285 magnetic susceptibility broadening.

286

287 Several convenient approaches to numerically determining the susceptibility fields inside and  
 288 outside volumes of different shapes.<sup>61,62</sup> One approach divides the local medium into finite  
 289 volume elements and the sum of all the different magnetic dipole field contributions. In a  
 290 simple case of small  $\chi \leq 1$  (as in most samples), the dipole field  $B_z$  can be expressed by an  
 291 angular dependence function,

$$292 \quad B_z(\theta, r) = \frac{\mu_0 m (3 \cos^2 \theta - 1)}{r^3} \quad (5)$$

293 where  $m$  is the individual magnetic moment,  $\theta$  is the angle of the dipole vector to  $B_0$ , and  $r$  is  
 294 the distance apart. Note that  $B_z$  determines the resonance shift, which leads to line  
 295 broadening, in the nuclear Larmor frequency induced by  $m$ , but it vanishes in the far distant  
 296 field or along the surface of a magic-angle cone,  $\cos^{-1}(1/\sqrt{3}) = 54.74^\circ$  to the external field.  
 297 This angle is significant for line-narrowing, which will be covered in a later section. A simple  
 298 numerical estimation of the  $B_z$  field can be deduced using an ideal spherical model (Figure  
 299 1a), where a magnetized sphere with a radius of  $a$  and a permeability  $\mu_{\text{sphere}} = 1 + \chi_{\text{sphere}}$   
 300 submerged in a sample with  $\mu_{\text{sample}} = 1 + \chi_{\text{sample}}$ . The different dipole fields dispersed outside  
 301 the magnetized sphere can be simplified as,

$$302 \quad B_z(\theta, r) \approx -\frac{\Delta\chi a^3}{3 r^3} B_0 (3 \cos^2 \theta - 1) \quad (6)$$

303 where  $\Delta\chi = \chi_{\text{sample}} - \chi_{\text{sphere}}$ . For example, the resonance frequency of the water molecules ( $\chi$   
 304  $= -9 \times 10^{-6}$  SI unit, the negative value indicates diamagnetism) in a water bath containing a  
 305 spherical air bubble ( $\chi \approx 0$ ) can shift as high as 6 ppm when  $r = a$ . This shift decreases as  $r$   
 306 increases, say to  $3a$ ; the shift is about 1.3 ppm, in-line with a typical linewidth of the water  
 307 resonance. A similar effect can be found in the metabolite protons residing around the  
 308 different cellular compartments, and each corresponds to a different magnetized sphere.

309

310 Another source of the  $B_z$  field is from the nearest probe components, which can be significant  
 311 in the  $\mu$ -size probe, where the entire sample volume is only a submillimeter apart from the  
 312 magnetized materials such as the microcoil. For example, Webb and Grant<sup>63</sup> have shown a

313 threefold increase in the linewidth when a nano-volume sample is centered inside the  
314 solenoid with only 50- $\mu\text{m}$  apart from the microcoil.

315

316 There are several approaches to suppress  $B_z$  ascribed to the coil. These include the use of a  
317 zero-susceptibility wire. It is a copper-alloy with a positive susceptibility metal, such as  
318 aluminum ( $\chi = +20.9 \times 10^{-6}$ )<sup>64</sup> or rhodium ( $\chi = +168 \times 10^{-6}$ ),<sup>65</sup> to cancel the negative  
319 susceptibility contribution of the copper. However, the cost of manufacturing zero-  
320 susceptibility wire is high because of the difficulty in producing precise and reproducible  
321 doping content with small diameter wires. An academic group has proposed a laboratory  
322 method of constructing a zero-susceptibility coil using a hollow copper capillary filled with a  
323 specific concentration of a paramagnetic solution  $\text{NiSO}_4$  neutralizing the negative  
324 susceptibility of copper.<sup>66</sup>

325

326 Another approach to minimize the  $B_z$  effects is to surround the microcoil with a cylindrical  
327 medium of matching susceptibility creating an infinite long uniform field around the sample  
328 to facilitate the field shimming. The medium can be a perfluorinated fluid such as FC-43 ( $\chi =$   
329  $-8.8 \times 10^{-6}$ ),<sup>14</sup> or an epoxy solid doped with a specific content of positive susceptibility  
330 paramagnetic ions.<sup>67,68</sup> The simplicity of these methods has accelerated the academic research  
331 on microcoil in liquid-state NMR for producing high-resolution spectral data.

332

333 ***Magic-angle spinning.*** As stated in Equation 5, the angular dependence  $B_z$  field vanishes  
334 when the dipole vector from the magnetic moment aligns with an axis at an angular distance  
335 of  $54.74^\circ$  to the external field. The angle is known as the magic-angle. This, in turn, suggests  
336 that spinning a sample at a magic-angle would eliminate the  $B_z$  field, suppressing the  
337 susceptibility broadening. This was first demonstrated in the early work of Garroway<sup>69</sup> with  
338 liquid samples and later discussed by Barbara<sup>70</sup> in detail of the demagnetization fields inside  
339 the small volume cylindrical samples (40  $\mu\text{L}$ ) at magic-angle, so-called the magic-angle  
340 cylinder. This essentially marked the beginning of the high-resolution standard magic-angle  
341 spinning technique, widely known as 'HR'-MAS. An extensive description of the theoretical  
342 and hardware of HR-MAS NMR can be found in ref 71 and 72. As illustrated in Figure 1b,  
343 when the sample rotates along the axis of magic-angle  $\theta_{MA}$ , the angle  $\delta$  and the azimuth angle  
344  $\phi$  become a time-dependent component given as:

345 
$$\cos\delta(t) = \cos\beta\cos\theta_{MA} + \sin\beta\sin\theta_{MA}\cos(\phi(t)) \quad (7)$$

346 where  $\beta$  is the angular separation between the sample rotation axis and the directional dipole  
 347  $D_r$ , and  $\phi$  is the azimuth angle on the plane perpendicular to the rotation axis. Integrating the  
 348 above Equation 7 with 5, the resultant  $B_z$  field of a rotating sample becomes

$$349 \quad B_z = \frac{\mu_0 m}{2r^3} \left\{ \begin{array}{l} (3\cos^2\beta - 1)(3\cos^2\theta_{MA} - 1) + \\ 3\sin 2\beta \sin 2\theta_{MA} \cos(\omega_r t + \phi) + \\ 3\sin^2\beta \sin^2\theta_{MA} \cos(2(\omega_r t + \phi)) \end{array} \right\} \quad (8)$$

350 where  $\omega_r$  is the sample rotation frequency. When  $\theta_{MA} = 54.74^\circ$ , the first term vanishes,  
 351 leaving the second and third terms as the spinning-sideband signals that appear at multiple  
 352 amplitude periods depending on the static linewidth of  $\omega_r = 0$ . Subsequently, MAS  
 353 eliminates the susceptibility broadening  $B_z$  at rapid spinning and results in isotropic  
 354 resonances at chemical shifts depending on the induced field driven by the chemical  
 355 shielding. MAS also eliminates – partially in some cases – other local susceptibility fields  
 356 ascribe from the spin interactions, such as spin-spin dipole, anisotropic chemical shift, and  
 357 quadrupole. These interactions can contribute up to kHz–MHz in linewidth for solids.  
 358 Therefore, fast sample rotation is imperative to characterize the local spin environments in  
 359 solid materials.

360

361 In the context of 'HR'-MAS, it is essential to note that MAS does not eliminate the  
 362 susceptibility  $B_z$  fields ascribed from the probe materials outside the rotating sample. For a  
 363 standard solid-state 4-mm MAS probe, the coil and stator (the closest components to the  
 364 sample) are about 1–2 mm apart from the sample located at the wall of the rotor. This  
 365 contributes to some degree of unsuppressed line broadening with the MAS. This is evident by  
 366 the skew baseline for each resonance acquired from a conventional 4-mm MAS probe (Figure  
 367 2). For microcoil MAS, the entire sample volume is merely a few hundredth microns apart  
 368 from the coil, which renders a significant  $B_z$  field and gives substantial broadening. An  
 369 example has been illustrated by an early attempt to profile a 150  $\mu\text{g}$  muscle tissue using a  
 370 sub-microcoil 1.6-mm MAS at 21 T.<sup>73</sup> Despite the excellent sensitivity, it is obtained at the  
 371 cost of susceptibility broadening from the probe materials and obscured the J-splitting for  
 372 metabolic identifications. As a result, only the lipid signals could be confidently identified.  
 373 Unquestionably, the first of many challenges in the microcoil MAS development toward  
 374 metabolomic applications is to achieve sufficient high spectral resolution without sacrificing  
 375 the sensitivity  $B_1/i$ .

376

377 **Toward high-resolution standard microcoil MAS**

378 Since the first demonstration of high-resolution standard MAS on liquid samples,<sup>69,70</sup>  
 379 academic and commercial groups have invested extensive resources in developing HR-MAS  
 380 probes to advance its application with high data reproducibility, user feasibility, and  
 381 accessibility. As a result, HR-MAS has become the principal technique in *ex vivo* NMR  
 382 studies of specimens like pathological biopsies.<sup>1-7</sup> On the contrary, the development of high-  
 383 resolution capable microcoil MAS is scarce. The first attempt on the submilligram sample  
 384 was with a bovine tissue (~300µg) using a spinning microcoil in 2007.<sup>18</sup> But, it was not until  
 385 2012 that an evaluation was made on profiling the metabolome on human tissue (<500 µg).<sup>31</sup>  
 386 The results demonstrated a gain in sensitivity *via* the microcoil, but the <sup>1</sup>H line resolution was  
 387 insufficient for metabolic profiling. Regardless, the results rendered a realization of an NMR  
 388 application on µg-scale tissues with microcoil MAS.

389  
 390 The technological issues and challenges for developing a microcoil MAS probe with a 'high-  
 391 resolution' capability are different than those for a microcoil (or ultrafast) MAS probe. While  
 392 faster sample spinning, stronger rf field, and reducing the frictional and electrical heating are  
 393 the prime interests in the ultrafast probe developments, the high-resolution probe focuses on  
 394 the high spectral resolution (down to ppb) capability with good feasibility and data  
 395 reproductivity and reliability. As expected, the complication in the microcoil probe  
 396 development is the complexity of handling the small size materials. A slight deviation or  
 397 error from the ideal condition – whether in the probe materials, microcoil, or NMR sample  
 398 preparation – will magnify its effect on the NMR performance and, therefore, on the spectral  
 399 resolution. To this day, the development of high-resolution standard microcoil MAS is still in  
 400 its infancy, and only proof-of-concept studies have been reported (Table 1).

401

402 Table 1. A chronological list of the significant developments that have led to 'HR' standard  
 403 microcoil MAS NMR

Year	Microcoil condition (active coil volume) <sup>a</sup>	Highlight	Result <sup>b</sup>
2006 <sup>[17]</sup>	Static (vary; sample volume down to 10 nL)	Introduced the first microcoil MAS probe: piggyback design	<ul style="list-style-type: none"> <li>–A µg sample capillary is piggybacked on a standard rotor</li> <li>–Enhanced <math>B_1/i</math> <i>via</i> the µcoil</li> <li>–Demonstrated the possibility of µg sample analysis</li> </ul>
2007 <sup>[18]</sup>	Spinning (vary <900 nL)	Introduced an inductive spinning resonator: MACS	<ul style="list-style-type: none"> <li>–An inductive resonator is placed inside a standard MAS rotor</li> <li>–Enhanced <math>B_1/i</math> <i>via</i> the inductive resonator; a mass-sensitivity of 46 mg<sup>-1</sup> is found for 750-µm MACS</li> </ul>

2012 <sup>[31]</sup>	Spinning (570 nL)	Evaluated the <sup>1</sup> H profiling with $\mu$ g biopsy using MACS	<ul style="list-style-type: none"> <li>–Insufficient <sup>1</sup>H line resolution for metabolic analysis</li> <li>–Carried out on an 870-<math>\mu</math>m diameter resonator with &lt;500 <math>\mu</math>g tissue</li> <li>–A 17-fold mass sensitivity enhancement compared to HR-MAS</li> <li>–Insufficient <sup>1</sup>H resolution (0.01 ppm)</li> <li>–Demonstrated the high versatility</li> <li>–Difficult in coil fabrication with no reproductivity</li> </ul>
2012 <sup>[75]</sup>	Spinning (500 nL)	Introduced an automated fabrication of MACS: on-chip MACS	<ul style="list-style-type: none"> <li>–Carried out on a 1000-<math>\mu</math>m diameter resonator</li> <li>–Eased the fabrication with a robotic wire-binding technology; ~100 resonators per production</li> <li>–Poor line resolution (1 ppm) ascribed to the large susceptibility gradient from the gold wire solenoid</li> <li>–Demonstrated the possibility of mass-manufactured resonators</li> </ul>
2013 <sup>[73]</sup>	Static (19300 nL)	Attempt on <sup>1</sup> H profiling of $\mu$ g-tissue using a standard MAS probe	<ul style="list-style-type: none"> <li>–Carried out on a 1.6-mm MAS with a 150 <math>\mu</math>g tissue at 21 T</li> <li>–Good sensitivity but with poor line resolution due to the strong magnetic susceptibility gradients from the stator and coil</li> </ul>
2013 <sup>[76]</sup>	Spinning (200 nL)	Refined the MACS design (First 'HR'-capable microcoil MAS)	<ul style="list-style-type: none"> <li>–Carried out on a 550-<math>\mu</math>m diameter resonator</li> <li>–Offered excellent <sup>1</sup>H resolution (0.004 ppm) while retaining the sensitivity</li> </ul>
2014 <sup>[77]</sup>	Spinning (vary: 100–420 nL)	A demonstrative metabolomic study on submillimeter organisms using HR-MACS (First metabolomic NMR study with nL volume under MAS)	<ul style="list-style-type: none"> <li>–First metabolomic NMR study with microcoil MAS</li> <li>–The model study was carried out with an 840-<math>\mu</math>m diameter resonator with samples of &lt;100 <i>C. elegans</i> individual</li> <li>–Introduced the use of a single fixed resonator with a sample-exchange capillary for easing the sample preparation</li> <li>–Successfully carried out the <sup>1</sup>H metabolic profiling and discrimination analysis of <i>C. elegans</i></li> <li>–Limited to small scale study due to coil fragility</li> <li>–Single worm detection was carried out with a 400-<math>\mu</math>m resonator</li> </ul>
2015 <sup>[78]</sup>	Static (<1500 nL)	Introduced a 'high-resolution' capable 1-mm microcoil MAS probe: HR- $\mu$ MAS	<ul style="list-style-type: none"> <li>–Modified from an ultrafast 1-mm MAS probe by replacing with a specific design stator</li> <li>–Despite the new stator, strong rf shimming fields are needed to acquire a good line resolution (0.002 ppm),</li> </ul>

			suggesting the presence of magnetic susceptibility gradients
			–Demonstrated the feasibility of 2D $^1\text{H}\{^{13}\text{C}\}$ HMQC experiment
2018 <sup>[79]</sup>	Static (<1500 nL)	–A demonstrative study on $\mu\text{g}$ food tissues using HR- $\mu\text{MAS}$	–First metabolomic NMR study with HR- $\mu\text{MAS}$ with a model study of $n>30$ with $\sim 300$ $\mu\text{g}$ tissue
			–Demonstrated a reliable metabolomic study with multivariate analysis for localizing the metabolic variances in different anatomical tissues
2019 <sup>[80]</sup>	Spinning (500 nL)	–Refined the on-chip MACS (Voxalytic <sup>TM</sup> MACS insert)	–Replaced the original gold wire with copper, resulting in a significant improvement in line-resolution (from 1 to 0.01 ppm); but still inferior to HR-MACS and HR- $\mu\text{MAS}$
2021 <sup>[81]</sup>	Static (<1500 nL)	–A demonstrative study on $\mu\text{g}$ rodent tissues using HR- $\mu\text{MAS}$ with a model study of $n>100$ (First metabolomic study on $\mu\text{g}$ tissue biopsy)	–Spatial metabolic mapping on tumoral brain slices –The large-scale study with $n>100$ of $\sim 300$ $\mu\text{g}$ tissue illustrated the capability of acquiring good reliability and reproducibility spectral data –Delimited the tumor lesion using multivariate analysis

404 (a) Estimated value from the solenoidal dimension; (b) line resolution were deduced from a sucrose  
405 resonance

406  
407 The first high-resolution capable microcoil MAS probe<sup>76</sup> was a modification of an early  
408 success ultrafast microcoil probe, which used an inductively coupled spinning  $\mu$ -resonator,  
409 so-called magic-angle coil spinning (MACS).<sup>18</sup> It is essentially a self-resonant solenoid coil  
410 wrapped closely around a nano-volume capillary and is secured inside a standard large MAS  
411 rotor. The setup renders an ensemble spinning to suppress the susceptibility  $B_z$  fields from the  
412 rotating microcoil and the sample and gain sensitivity *via* the inductively coupled microcoil.  
413 One advantage of MACS is the resonator's dimensions versatility. It enables tailoring the  
414 active and sample volume to accommodate the optimum filling factor. However, the spinning  
415 of a coil under a magnetic field inherently generates an eddy current within the conductive  
416 wire, producing heat *via* the dissipated power. The power can be estimated by modeling a  
417 single rotating loop of a conductive wire,<sup>82</sup>

$$418 \quad P = \omega_r^2 B^2 \left( \frac{r h^3 w}{\rho} \right) \quad (9)$$

419 It depends on various factors: the effective magnetic field ( $B$ ), the rotating frequency ( $\omega_r$ ),  
420 the loop radius ( $r$ ), and the wire cross-section ( $w$ ), and its resistivity ( $\rho$ ). Any increase of  
421 these factors would lead to a rise in power and thus increase sample heating. This was evident  
422 with a microcoil constructed with a 62- $\mu\text{m}$  cross-section of a Cu wire, spinning at 6000 Hz

423 inside an 11.7 T magnet;<sup>76</sup> it heated the sample by 37 °C. In contrast, the heating decreased to  
424 1.6 °C with a thinner 30-µm Cu wire; and it further reduced to 0.02 °C with a reduced  
425 spinning frequency to 500 Hz. Indeed sample heating is of concern, not only to the integrity  
426 of the specimens, but it generates a temperature gradient throughout the sample volume and  
427 subsequently gives rise to line broadening caused by a series of frequency shifts in the  
428 resonance.<sup>83</sup> The consequences can be severe for a water (HDO) sample since the <sup>1</sup>H  
429 chemical shift is temperature-dependence -11.9 ppb/°C.<sup>84</sup> Figure 3 shows a dramatic loss of  
430 the sucrose anomeric proton line resolution as the spinning frequency increases. This is  
431 mainly attributed to the heating originating from the eddy current arising in the spinning Cu  
432 wire. For example, at a routine 5000 Hz spinning, it generates about 2 °C, efficiently  
433 concealing a J-splitting of 4 Hz. In contrast, a clear doublet is well resolved with low  
434 spinning (<500 Hz), but it gives rise to a dense spinning-sideband pattern in the spectrum  
435 (Equation 8), and requires suppression pulse experiments to disclose the isotropic resonances.  
436 The refined MACS design – thin wire coil with slow-spinning – to achieve high-resolution  
437 capable microcoil MAS is referred to as HR-MACS.

438

439 HR-MACS had shown an impressive spectral quality for profiling the metabolome with only  
440 12-individuals of the submillimeter nematodes *Caenorhabditis elegans* (Figure 4).<sup>77</sup> The  
441 spectral similarity to the large volume HR-MAS with more than 1000 individuals is  
442 unprecedented. It rendered the identification of a total of 31 metabolites, representing the  
443 most NMR-identified metabolites in a MAS spectrum of a nano-volume biological sample.  
444 The sensitivity enhancement with HR-MACS is 5-fold ( $B_1^{HRMACS} / B_1^{HRMAS}$ ) higher than that  
445 with HR-MAS. In other words, it would require an acquisition period of 25× longer for HR-  
446 MAS to obtain the same level of SNR as for HR-MACS with 12-individual worms. Pushing  
447 the sensitivity limit, HR-MACS identified a few metabolite signals from a single  
448 submillimeter worm at 18.8 T. However, the resultant spectral resolution was poor due to a  
449 field drift over the 10-h acquisition. Regardless, the result offered a glimpse of the possibility  
450 for a MAS study of a single tiny organism. This study also illustrated the beneficial factor of  
451 analyzing a few numbers of the organism. To avoid crowding in the cultivation progress,  
452 about 100 (or fewer) individuals are cultivated in a single culture plate; this would require 10  
453 plates to cultivate 1000 individuals for a single NMR sample for HR-MAS. As a result, a  
454 single model study with HR-MAS would require a demanding cultivation procedure.<sup>85</sup> On the  
455 other hand, with the possibility of analyzing a few individuals, one plate would allow

456 multiple NMR samples, dramatically reducing the cultivation procedures. This was  
457 demonstrated by a discrimination analysis (OPLS-DA) of two finite *C. elegans* groups (wild-  
458 type vs *slcf-1*) with <100 individuals.<sup>77</sup>

459

460 One issue with HR-MACS is the fabrication of the tiny and fragile LC circuitry of the  $\mu$ -  
461 resonator. It demands high-precision procedures. The current effective method is manually  
462 winding, which is a labor-intensive process with zero reproductivity. To ensure the spectral  
463 reproducibility for multivariate analysis, our team introduced the use of a single  $\mu$ -resonator  
464 permanently fixed inside a MAS rotor and permitting a sample screening with a smaller  
465 diameter sample capillary. Two metabolomic studies with multivariate statistics have been  
466 performed with this setup,<sup>77,86</sup> illustrating the potential in metabolomic studies. However, the  
467 constant severe spinning stress exerted onto the resonator is limited to small model studies.

468

469 Several reports have acknowledged the difficulty in assembling and reproducing the  $\mu$ -  
470 resonators and have attempted to apply different manufacturing approaches to ease the  
471 fabrications. Korvink and his team exploited the automation of a robotic wire-bonding  
472 technology to wind an  $\mu$ -solenoid and bind to a capacitor chip. They denoted the resonator as  
473 on-chip MACS.<sup>75</sup> The fabrication process is carried out entirely by a robotic wire-bonding  
474 apparatus, enabling to produce 100 on-chip MACS resonators in a single procedure. However,  
475 the reported NMR linewidth was highly inadequate, with about 1 ppm. This was due to the  
476 significant susceptibility mismatched from the gold wire ( $\chi = -34 \times 10^{-6}$ ) used in the wire-  
477 bonding. Later, a significant improvement was made on the line-resolution, from 1 ppm to  
478 about 0.01 ppm, by replacing the gold wire with copper,<sup>86</sup> and thereafter, it was  
479 commercialized as Voxalytic<sup>TM</sup> MACS insert. Another MACS design, the so-called  
480 monolithic MACS, was later introduced.<sup>87</sup> The design is based on a planar transmission-line  
481 resonator, which is self-resonant and does not require lumped-element capacitors, permitting  
482 the use of 2D MEMS printing technology. Although the manufacturing was less efficient than  
483 the wire-bonding, it offered a line resolution of about 0.1 ppm. Regardless, these studies  
484 demonstrated the possibility of mass-production of  $\mu$ -resonators for MACS. It is now a  
485 matter of minimizing the susceptibility mismatched with the samples to improve line  
486 resolution.

487

488 In 2015, a new high-resolution standard microcoil probe was introduced,<sup>78</sup> denoted as HR-  
 489  $\mu$ MAS. Unlike the spinning microcoil in HR-MACS, the new probe consists of a solenoid  
 490 with 1-mm in diameter incorporated inside the MAS stator with a 490 nL sampling volume.  
 491 A few probe components near the sampling volume were of significant concern in the probe  
 492 design to retain the high-resolution spectra. For example, to reduce the induced  $B_z$  fields, the  
 493 microcoil is wound with a zero-susceptibility wire (Cu/Al), the air-bearings are made of a  
 494 susceptibility-matched Vespel ( $\chi = -9.2 \times 10^{-6}$ ), similarly the entire stator structure is made  
 495 with Kel-F ( $\chi = -11.6 \times 10^{-6}$ ). As shown in Figure 5, these modifications have significantly  
 496 improved the linewidth at 50% height (FWHM), but it also exhibits a significant skew line at  
 497 1% height. Based on a numerical field map simulation, the skew line is ascribed from the two  
 498 Vespel air-bearings inside the Kel-F stator generating a strong unwanted quadratic field to the  
 499 sample volume.<sup>88</sup> To overcome this, a pair of passive ferro-shim was strategically integrated  
 500 inside the probehead (Figure 5) to offset the unwanted field and supplement additional shim  
 501 field equivalent to the active shim field of  $B_{x^2-y^2}$ , which in turn produces a quadratic field at  
 502 magic-angle  $B_{z^2}^{MAS}$

$$503 \quad B_{z^2}^{MAS} = B_{x^2-y^2} - 2\sqrt{2}B_{zy} \quad (10)$$

504 where  $B_{x^2-y^2}$  and  $B_{zy}$  are the harmonic field functions in the active NMR shims. This  
 505 implementation has suppressed the unwanted perturbed fields and yielded high-resolution  
 506 spectra.

507

508 In contrast to HR-MACS, HR- $\mu$ MAS is a highly versatile and robust probe with the  
 509 feasibility of heteronuclear experiments.  $^1\text{H}$ - $^{13}\text{C}$  HMQC experiment has been performed to  
 510 profile the lactate and its brain physiological metabolism from a  $\sim 300 \mu\text{g}$  brain tissue  
 511 extracted from a rat model previously infused with  $[3-^{13}\text{C}]\text{lactate}$  during a brain simulation.  
 512 Despite the long acquisition (27 hr), a few metabolites (alanine, lactate, glutamate, glutamine,  
 513 and  $\gamma$ -aminobutyric acid) were identified as the relevant brain lactate metabolism accordant  
 514 with those found in a previous HR-MAS study.<sup>89</sup>

515

516 The first complete study of NMR-based metabolomics with the HR- $\mu$ MAS probe was carried  
 517 out on a  $\sim 300 \mu\text{g}$  tissue sampling of *Allium sativum* (garlic, Figure 6).<sup>79</sup> This study highlights  
 518 a significant ex vivo NMR application with small size sampling. It enables the investigation  
 519 of small anatomical regions that would be impractical with mg-scale sampling using HR-  
 520 MAS. Specifically, a total of 14 metabolic variances, including the organosulfur compound

521 cycloallicin, has been identified in the two small sub-tissue anatomies (sprout and inner  
522 epidermis) inside the garlic core.

523

524 A subsequent study explored the potential of rodent tissue biopsy by spatially profiling across  
525 a coronal brain slice of C6 gliomas bearing.<sup>81</sup> Figure 7 shows that with the same acquisition  
526 time, 13-min, the resultant line resolution of HR- $\mu$ MAS is *on par* with that of HR-MAS; but  
527 with nearly 30-fold less in the tissue mass. In addition, the high-resolution spectra data permit  
528 unambiguous identification of the NMR markers of C6 gliomas in the rat models. The small  
529 sampling mass permitted a systematic metabolic mapping across the brain slice with a  
530 volume voxel of  $1 \times 1 \times 3 \text{ mm}^3$ , rendering a delineation of the tumor lesion using a linear PLS  
531 regression and a semi-quantification analysis. Thus, the study presents a unique *ex vivo* NMR  
532 possibility for analyzing pathological tissue. Another aspect worth noting is that it applied a  
533 high number of sampling data (nearly a 100-sample) in the model study, illustrating the  
534 capability to acquire reliable and consistent data with the HR- $\mu$ MAS probe for advanced  
535 multivariate statistics. Indeed, this is imperative for metabolomic studies. Note that this large  
536 sampling model would not be possible with the previously discussed spinning  $\mu$ -resonator  
537 probe.

538

### 539 **Future prospects**

540 Although advancements have been made on the high-resolution standard microcoil MAS  
541 probe, it has yet to be widely applied in metabolomics. This is mainly due to the lack of  
542 feasibility. The main challenge lies mainly in the minuscule sample, which limits detection  
543 sensitivity and sample preparation. Further developments are necessary to continue striving  
544 forward to a level of application *on par* with the conventional HR-MAS NMR spectroscopy.

545

546 **Technical developments.** It should be noted that the current state of the microcoil is close to  
547 achieving the limit for detection sensitivity. Further improvement by orders of magnitude is  
548 not expected through  $B_1/i$ . Therefore, higher sensitivity would be achieved by incorporating  
549 other enhancement schemes. As discussed previously, high magnetic fields would enhance  
550 the sensitivity, but at the expense of the equipment and its running cost; moreover, it would  
551 also increase the susceptibility broadening ascribed to the microcoil. Increasing the signal-  
552 averaging would also increase the sensitivity by a factor of  $\sqrt{\text{scan}}$ , but it could demand an  
553 unrealistic acquisition period. Hyperpolarization techniques could be a possible route, but

554 how to incorporate the respective strategies is not apparent. Cryoprobe technology is  
555 probably the most viable; the main issue is implanting a thermal barrier between the cold  
556  $\mu$ coil and the ambient sample, complicated by the MAS stator. The piggyback concept<sup>17</sup>  
557 could offer a possible solution where the stator is segregated from both the microcoil and the  
558 sample and could ease the implementation of an isolated cold coil. Moreover, the sample is  
559 no longer constrained inside a rotor, allowing an elongated sampling volume that renders a  
560 long ellipsoid field to facilitate the field shimming. The segregation of the sample from the  
561 stator could also offer a more feasible solution to the NMR-sample preparation.

562

563 Sample preparation is a critical component in all bioanalytical methods. Standardized  
564 protocols are necessary and have been well-established in most *ex vivo* NMR-based  
565 applications.<sup>90-92</sup> This is not the case for microcoil MAS. Sample preparation for the NMR  
566 analysis may seem trivial at first glance, but it is, in fact, a strenuous task for handling  
567 specimens at a minuscule level. One must consider the entire procedure clean and quick for  
568 preserving the sample integrity. The necessity of using a  $\mu$ -size sample-holder requires a  
569 filling procedure that can be strenuous. The current most efficient methods are simply using a  
570 micro-pipette for the solution and sampling punch for tissue with a centrifuge,<sup>93</sup> but these  
571 procedures are slow and demanding. Acknowledging the difficulty, the use of sampling glass  
572 capillary has been proposed for the spinning resonator HR-MACS<sup>77</sup> and the HR- $\mu$ MAS  
573 probe.<sup>94</sup> The advantage is that it permits the NMR-sample preparation outside the rotor,  
574 simplifying the sample filling procedure. The trade-off is the loss of sensitivity with a  
575 reduced coil filling factor that can be down to 50% depending on the capillary thickness.  
576 Disposable Kel-F rotor (similar concept to the Bruker Kel-F bioinsert) has also been  
577 considered for HR- $\mu$ MAS probe,<sup>78,94</sup> but the fragility of the small plastic rotor has hindered a  
578 rapid preparation. Indeed, further improvement is essential for a more feasible analysis with  
579 the microcoil probe. This may require new devices, such as microfluidic, for simplifying the  
580 sample filling or even an entirely new design of the microcoil probe that can facilitate the  
581 entire preparation. For example, one could consider the piggyback design,<sup>17</sup> in which the  
582 sample tube is segregated from the rotor and could be manipulated or coupled with external  
583 sample-filling apparatus.

584

585 **Possible applications.** The prime advantage of microcoil MAS probes is that it opens the  
586 possibility of analyzing samples with limited availabilities. These can be biospecimens such

587 as tissue biopsies, cells, organisms, or aggregated biomolecules, and they can also be non-  
588 biosamples such as polymeric resins. It offers the investigations of a specific phenotype in  
589 isogenic specimens that would be impractical with HR-MAS because of the difficulty of  
590 isolating a sufficient quantity of the target specimens. For example, in the cell biology field,  
591 'HR' standard microcoil MAS would be able to explore the metabolomes in target cell-type,  
592 an emerging research area in mass spectrometry that can provide a fundamental prerequisite  
593 metabolic information for understanding the underlying functions and activities. Unlike cell  
594 culture, isolating the target cell type directly from an animal is a daunting task; it relies on  
595 specific cell sorting techniques, which often hinder the collection of large quantities  
596 necessary for the profiling with HR-MAS. For example, profiling the isolated neuron and  
597 astrocyte cells may help yield insights into the fundamental of intercellular metabolic  
598 cooperation between neurons and astrocytes to further understand brain metabolism.<sup>95</sup>

599

600 Another advantage is the possibility of analyzing tiny spatial tissue regions, allowing a direct  
601 characterization of the metabolite in question that can be concealed in large sampling tissue  
602 mass. For example, a recent *ex vivo* HR-MAS study<sup>96</sup> of epilepsy with a kainate-injected  
603 epileptic mouse model reported an increased  $\gamma$ -aminobutyric acid (GABA) level in the entire  
604 ipsilateral anterior region of the hippocampus, eliciting the relevancy of GABA as a  
605 biomarker of the epileptogenic zone. However, the extensive sampling tissue mass (5 mg)  
606 made it impossible to delineate further the epileptic zone within the region. Figure 8 shows an  
607 example of benefiting the small spatial analysis (with  $\sim 150$   $\mu\text{g}$  sampling) using the HR-  
608  $\mu\text{MAS}$  probe; it reveals an increased level of GABA in a tiny subregion (dentate gyrus) of the  
609 ipsilateral anterior hippocampus, pinpointing the epileptic location. Although the result needs  
610 further confirmation, it illustrates the underlying benefit of  $\mu\text{g}$  sampling over the mg scale.

611

612 In health science, small sample analysis could be used as a complementary approach to  
613 advanced imaging techniques for enhancing the recognition of the modified metabolic  
614 patterns of the disease in tissue. The potential of firsthand monitoring of the perturbations in  
615 metabolic responses of the diseases could offer a practical and immediate treatment, opening  
616 the possibility in clinical NMR spectroscopy, a concept proposed by Nicholson.<sup>97</sup> Moreover,  
617 the current gold standard in clinical tissue assessment is histopathology. When the tissue  
618 mass is limited in a single biopsy, the mg tissue analysis with HR-MAS can be complicated  
619 as it can compromise the histopathological assessments; but this would not be the case with

620 microcoil MAS. In addition, the excision of  $\mu\text{g}$  tissue from a human patient or animal could  
621 reduce surgical invasiveness and permit longitudinal studies.

622

623 In agricultural science, the analysis with  $\mu\text{g}$  samples could provide direct insights into the  
624 integration and regulation of plant metabolism: from a single seed to a grown plant. For  
625 example, the germination process in a seed is complex and of great importance for  
626 developing the plant seeds to form a new individual. To characterize the metabolic  
627 coordination of the distinct small regions in a seed could help the development of  
628 germination<sup>98</sup> and essentially the plant growth. This could benefit from a spatiotemporal  
629 analysis on a single seed.

630

### 631 **Conclusion**

632 The recent developments of high-resolution standard microcoil MAS probe technology have  
633 offered the opportunity for opening new applications in the *ex vivo* platform of NMR-based  
634 metabolomics. However, there is no question that further improvements in NMR sensitivity  
635 and sample preparation are necessary for routine analysis of  $\mu\text{g}$  specimens and venture into  
636 clinical NMR spectroscopy. We are convinced that 'HR'- $\mu\text{MAS}$  NMR analysis could become  
637 an important component in the omics research, but this would take a collaborative effort  
638 among the different disciplines with complementary expertise to continue advancing and  
639 making high-resolution standard microcoil MAS a real possibility in metabolomics and omics  
640 in general.

641

642 **Funding:** The developments presented here are supported by Agence Nationale de la  
643 Recherche in France (ANR-16-CE11-0023 and ANR-12-JSV5-0005)

644 **Acknowledgments:** I would like to acknowledge the undivided supports from all  
645 collaborators, including JEOL Resonance Inc. on the HR- $\mu\text{MAS}$  probe. Dr Florence Fauvelle  
646 (GIN, France) is also acknowledged for the preliminary unpublished results on the epilepsy  
647 tissue in Figure 8.

648 **Conflicts of Interest:** The authors declare no conflict of interest.

649 **Data availability:** All of our works present in the review are available from the  
650 corresponding author upon reasonable request.

651

652

653 **Figure Captions**

654 **Figure 1.** (a) Magnetic dipole field  $B_z$  at point P of the sample ( $\mu_{\text{sample}}$ ) region outside of a  
655 magnetized sphere ( $\mu_{\text{sphere}}$ ), of which it has a radius of 'a' and a dipolar magnetic moment m  
656 induced by the external NMR field  $B_0$ .  $\delta$  is the angle between  $B_0$  and the dipolar vector  $D_r$ ,  
657 which depends on a distance r between m and P. (b) The MAS effect, where  $\delta$  becomes a  
658 time-dependent component  $\delta(t)$  with a magic-angle  $\theta_{\text{MA}} = 54.74^\circ$ , and  $\beta$  is the angle between  
659 the direction of the rotation axis and  $D_r$ . and  $\phi$  is the azimuth angle characterizing the  
660 position of a magnetic moment m in a plane perpendicular to the rotation axis.

661  
662 **Figure 2.**  $^1\text{H}$  spectral comparison of sucrose in  $\text{D}_2\text{O}$  at 11.7 T between solid-state MAS  
663 probes and high-resolution capable MAS probes. The arrow depicts the development toward  
664 high spectral resolution capable without forfeiting the detection sensitivity.

665  
666 **Figure 3.** (a)  $^1\text{H}$  doublet of an anomeric proton in sucrose, illustrating the loss of line  
667 resolution as the MAS frequency increases with a spinning resonator HR-MACS. (b) A  
668 summary of the FWHM in (a) and its estimated heat dissipation. The employed spinning  
669 resonator was constructed with a 30- $\mu\text{m}$  cross-section Cu wire. Adapted with permission  
670 from ref 76. Copyright 2013 American Chemical Society. Note that the temperature  
671 dependence on the chemical shift of the anomeric proton has also been observed in HR-  
672 MAS.<sup>83</sup>

673  
674 **Figure 4.**  $^1\text{H}$  spectral comparison at 18.8 T between HR-MACS and HR-MAS of *C. elegans*.  
675 Despite a drastic reduction of the worm individuals in HR-MACS, the chemical shift  
676 expansion showcases the detailed similarity in the resonance profile. Adapted with  
677 permission from ref 77. Copyright 2014 American Chemical Society.

678  
679 **Figure 5.** (a) Improvement of the line resolution with a pair of passive ferro shims mounted  
680 near the MAS stator. The  $^1\text{H}$  spectra of sucrose in  $\text{D}_2\text{O}$  were acquired at 11.7 T spinning at  
681 4000 Hz. (b) The numerical field simulation results show the 1D magnetic flux profile within  
682 the active sample along the magic-angle axis ascribed by the cylindrical bearings inside the  
683 stator ( $B_{\text{bearing}}$ ), a pair of ferro-shims ( $B_{\text{passive}}$ ), and the combined effect ( $B_{\text{sum}}$ ). The red  
684 highlight represents the sample region along the magic-angle axis  $Z'$ . Adapted with  
685 permission from ref 88. Copyright 2019 Springer Nature.

686  
687 **Figure 6.** (a)  $^1\text{H}$  spectral comparison of the different anatomical garlic regions between HR-  
688 MAS and HR- $\mu\text{MAS}$ . (b) The resultant S-line plot was used to identify the metabolite  
689 variances between the garlic core's two sub-regions (sprout and inner epidermis). A result  
690 that could not be easily deduced by the large-volume sampling HR-MAS experiments.  
691 Adapted with permission from ref 79. Copyright 2018 American Chemical Society.

692  
693 **Figure 7.** (a)  $^1\text{H}$  spectral comparison of the rat brain tissue between HR-MAS and HR- $\mu\text{MAS}$   
694 NMR at 11.7 T: black-line corresponds to HR-MAS of the tumoral (C6-glioma) lesion tissue,  
695 red and blue correspond to HR- $\mu\text{MAS}$  of the tumoral and healthy tissue, respectively. The  
696 spectral amplitudes are normalized to the tCr resonance. Based on the total SNR (1.0–4.2  
697 ppm), the mass-sensitivity per unit time for those acquired with HR- $\mu\text{MAS}$  is about 3-fold  
698 higher than HR-MAS. The significant NMR-markers are annotated with arrows indicating the  
699 increased and decreased level: red corresponds to tumoral tissue and blue healthy. (b) A PCA  
700 score plot was obtained from a model study containing 90-sampling data on brain tissue, 34  
701 from a single healthy brain slice, and 56 from two tumor-bearing slices. The excellent quality

702 parameters indicated the reliability of model data acquired by the HR- $\mu$ MAS probe. (c)  
703 Resultant analytical maps: [left] PLS-regression map showing the delineation of the tumor  
704 lesion. The level of the predicted values is coded with a color scheme: red being 1  
705 corresponds to tumoral tissue and blue being 0 to healthy tissue; [right] metabolite  
706 distribution map of tCho/NAA across the slice. Each color square in both maps is relevant to  
707 a  $1 \times 1$  sampling pixel. Adapted with permission from ref 81. Copyright 2021 John Wiley and  
708 Sons.

709  
710 **Figure 8.** *Ex vivo* localized  $^1\text{H}$  HR- $\mu$ MAS spectra of the three regions (dentate gyrus (DG)  
711 dispersion and cornu ammonis (CA1 & 3)) in an ipsilateral anterior of the hippocampus of a  
712 kainic acid-mesiotemporal lobe epilepsy mouse model, with a sampling mass of  $\sim 150$   $\mu\text{g}$ .  
713 Similar to the result in Figure 7, the mass-sensitivity per unit time for HR- $\mu$ MAS is about 3-  
714 fold higher than HR-MAS. This is an unpublished preliminary result. The spectral result  
715 demonstrates the beneficiary of  $\mu\text{g}$ -sampling with HR- $\mu$ MAS over mg-sampling with HR-  
716 MAS that has concealed the spatial origin of the evaluated GABA level.

717  
718

719 **References**

- 720 1. Kaebisch E, Fuss TL, Vandergrift LA, et al. Applications of high-resolution magic angle  
721 spinning MRS in biomedical studies I—cell line and animal models. *NMR Biomed*  
722 2017;e3700.
- 723 2. Dietz C, Ehret F, Palmas F, et al. Applications of high-resolution magic angle spinning  
724 MRS in biomedical studies II—human diseases. *NMR Biomed* 2017;e3784.
- 725 3. Lindon JC, Beckonert OP, Holmes E, Nicholson JK. High-resolution magic angle  
726 spinning NMR spectroscopy: application to biomedical studies. *Prog Nucl Magn Reson*  
727 *Spectrosc* 2009;55:79–100.
- 728 4. Sitter B, Bathen TF, Tessem M-B, Gribbestad IS. High-resolution magic angle spinning  
729 (HR-MAS) MR spectroscopy in metabolic characterization of human cancer. *Prog Nucl*  
730 *Magn Reson Spectrosc* 2009;54:239–254.
- 731 5. Bathen TF, Sitter B, Sjøbakk TE, et al. Magnetic resonance metabolomics of intact tissue  
732 a biotechnological tool in cancer diagnostics and treatment evaluation. *Cancer Res*  
733 2010;70:6692–6696.
- 734 6. Somashekar BS, Kamarajan P, Danciu T, et al. Magic angle spinning NMR-based  
735 metabolic profiling of head and neck squamous cell carcinoma tissues. *J Proteome Res*  
736 2011;10:5232–5241.
- 737 7. Tripathi P, Somashekar BS, Ponnusamy M, et al. HR-MAS NMR tissue metabolomic  
738 signatures cross-validated by mass spectrometry distinguish bladder cancer from benign  
739 disease. *J Proteome Res* 2013;12:3519–3528.
- 740 8. Bruker. Released the iProbe™ HRMAS at European Magnetic Resonance Meeting  
741 (EUROMAR), Nantes, France, 2018.
- 742 9. Van de Plas R, Yang J, Spraggins J, Caprioli RM. Image fusion of mass spectrometry  
743 and microscopy: a multimodality paradigm for molecular tissue mapping. *Nat Methods*  
744 2015;12:366–372.
- 745 10. Taylor L, Fuss BA, Cheng LL. Metabolic Imaging in Humans. *Topic in Magn Reson*  
746 *Imaging* 2016;25:223–235.
- 747 11. Zhu A, Lee D, Shim Hyunsuk. Metabolic Positron Emission Tomography Imaging in  
748 Cancer Detection and Therapy Response. *Semin Oncol* 2011;38:55–69.
- 749 12. Markley JL, Brüschweiler R, Edison AS, et al. The future of NMR-based metabolomics.  
750 *Curr Opin Biotechnol* 2017;43:34–40.
- 751 13. Comi TJ, Do TD, Rubakhin SS, Sweedler JV. Categorizing cells on the basis of their  
752 chemical profiles: progress in single-cell mass spectrometry. *J Am Chem Soc*  
753 2017;139:3920–3929.
- 754 14. Olson DL, Peck TL, Webb AG, et al. High-resolution microcoil <sup>1</sup>H NMR for mass-  
755 limited, nanoliter-volume samples. *Science* 1995;270:1967–1970.
- 756 15. Kc R, Henry ID, Park GHJ, Raftery D. New solenoidal microcoil NMR probe using  
757 zero-susceptibility. *Concepts Magn Reson Part B Magn Reson Eng* 2010;17:13–19.

- 758 16. Grimes JH, O'Connell TM. The application of micro-coil NMR probe technology to  
759 metabolomics of urine and serum. *J Biomol NMR* 2011;49:297–305.
- 760 17. Janssen H, Brinkmann A, Van Eck ERH, et al. Microcoil high-resolution magic angle  
761 spinning NMR spectroscopy. *J Am Chem Soc* 2006;128:8722–8723.
- 762 18. Sakellariou D, Goff G Le, Jacquinet J-F. High-resolution, high-sensitivity NMR of  
763 nanolitre anisotropic samples by coil spinning. *Nature* 2007;447:694–697.
- 764 19. JEOL Resonance Inc. Released a 0.75-mm  $\mu$ MAS probe. 53<sup>rd</sup> Experimental Nuclear  
765 Magnetic Resonance Conference (ENC), Miami, USA, 2012.
- 766 20. Bruker. Released Magic Angle spinning above 100 kHz. 56<sup>th</sup> Experimental Nuclear  
767 Magnetic Resonance Conference (ENC), Pacific Grove, USA, 2015.
- 768 21. Samoson A. H-MAS. *J Magn Reson* 2019;306:16–172.
- 769 22. Struppe J, Quinn CM, Lu M. et al. Expanding the horizons for structural analysis of fully  
770 protonated protein assemblies by NMR spectroscopy at MAS frequencies above 100  
771 kHz. *Solid State Nucl Magn Reson* 2017;87:117–125.
- 772 23. Struppe J, Quinn CM, Sarkar S, et al. Ultrafast 1H MAS NMR crystallography for  
773 natural abundance pharmaceutical compounds. *Mol Pharmaceutics* 2020;17:674–682
- 774 24. Paepé D C-D, Stanek J, Jaudzems K, et al. Is protein deuteration beneficial for proton  
775 detected solid-state NMR at and above 100 kHz magic-angle spinning? *Solid State Nucl*  
776 *Magn Reson* 2017;87:124–136.
- 777 25. Zhang R, Pandey MK, Nishiyama Y, Ramamoorthy A. A novel high-resolution and  
778 sensitivity-enhanced three-dimensional solid-state NMR experiment under ultrafast  
779 magic angle spinning conditions. *Sci reports* 2015;5:1181.
- 780 26. Zhang R, Mroue KH, Ramamoorthy A. Proton-based ultrafast magic angle spinning  
781 solid-state NMR spectroscopy. *Acc Chem Res* 2017;4:1105–1113.
- 782 27. Andreas LB, Jaudzems K, Stanek J, et al. Structure of fully protonated proteins by  
783 proton-detected magic-angle spinning NMR. *Proc Natl Acad Sci USA* 2016;113:9187–  
784 9192.
- 785 28. Penzel S, Oss A, Org ML, et al. Spinning faster: protein NMR at MAS frequencies up to  
786 126 kHz. *J Biomol NMR* 2019;73:19–29.
- 787 29. Schubeis T, Marchand TLe, Andreas L, Pintacuda G. <sup>1</sup>H magic-angle spinning NMR  
788 evolves as a powerful new tool for membrane proteins. *J Magn Reson* 2018;287:140–152
- 789 30. Loquet A, Mammeri NE, Stanek J. 3D structure determination of amyloid fibrils using  
790 solid-state NMR spectroscopy. *Methods* 2018;138-139:26–38
- 791 31. Wong A, Jiménez B, Li X, et al. Evaluation of high resolution magic-angle coil spinning  
792 NMR spectroscopy for metabolic profiling of nanoliter tissue biopsies. *Anal Chem*  
793 2012;84:3843–3848.
- 794 32. Hoult DI, Richards RE. The signal-to-noise ratio of the nuclear magnetic resonance  
795 experiment. *J Magn Reson* 1976;24:1969–1992.

- 796 33. Luchinat E, Barbieri L, Cremonini M, Banci L. Protein in-cell NMR spectroscopy at 1.2  
797 GHz. *J Biomol NMR* 2021;75:97–107.
- 798 34. Ardenkjaer-Larsen JH. On the present and future of dissolution-DNP. *J Magn Reson.*  
799 2016;264:2–12.
- 800 35. Thankamony ASL, Wittmann JJ, Kaushik M, Corzilius B. Dynamic nuclear polarization  
801 for sensitivity enhancement in modern solid-state NMR. *Prog Nucl Magn Reson*  
802 *Spectrosc* 2017;102/103:120–195.
- 803 36. Rossini AJ, Zagdoun A, Lelli M, et al. Dynamic nuclear polarization surface enhanced  
804 NMR Spectroscopy. *Acc Chem Res* 2013;46:1942–1951
- 805 37. Owers-Bradley JR, Horsewill AJ, Peat DT, et al. High polarization of nuclear spins  
806 mediated by nanoparticles at millikelvin temperatures. *Phys Chem Chem Phys*  
807 2013;15:10413–10417,
- 808 38. Spence MM, Rubin SM, Dimitrov IE, et al. Functionalized xenon as a biosensor. *Proc*  
809 *Natl Acad Sci USA* 2001;98:10654–10657.
- 810 39. Kuch LT. Photo-CIDNP NMR spectroscopy of amino acids and proteins. *Top Curr*  
811 *Chem* 2013;338:229–300
- 812 40. Duckett SB, Mewis RE. Application of parahydrogen induced polarization techniques in  
813 NMR spectroscopy and imaging. *Acc Chem Res* 2012;45:1247–1257.
- 814 41. Kovacs H, Moskau D, Spraul M. Cryogenically cooled probes – a leap in NMR  
815 technology. *Prog Nucl Magn Reson Spectrosc* 2005;46:131–155.
- 816 42. Brey WW, Edison AS, Nast RE, et al. Design, construction, and validation of a 1-mm  
817 triple-resonance high-temperature-superconducting probe for NMR. *J Magn Reson.*  
818 2006;179:290–293.
- 819 43. Mizuno T, Hioka K, Fujioka K, Takegoshi K. Development of a magic-angle spinning  
820 nuclear magnetic resonance with a cryogenic detection system for sensitivity  
821 enhancement. *Rev Sci Instrum* 2008;79:044706.
- 822 44. Hassan A, Quinn CM, Struppe J, et al. Sensitivity Boosts by the CPMAS CryoProbe for  
823 Challenging Biological Assemblies. *J. Magn. Reson.* 2020;311:106680.
- 824 45. Staab JP, Novak GJ, Kini S, Spitzmesser JB, Entzminger G, Holte LL, Doty FD.  
825 Development of a cryo-coil HR-MAS-PFG NMR probe for high-field WB magnets. 44<sup>th</sup>  
826 Experimental Nuclear Magnetic Resonance Conference (ENC), Savannah, 2003.
- 827 46. Webb AG. Radiofrequency microcoils in magnetic resonance. *Prog Nucl Magn Reson*  
828 *Spectrosc* 1997;31:1–42.
- 829 47. Minard KR, Wind RA. Solenoidal microcoil design–Part I: optimizing rf homogeneity  
830 and coil dimensions. *Concepts Magn Reson* 2001;13:128–142.
- 831 48. Minard KR, Wind RA. Solenoidal microcoil design–Part II: optimizing winding  
832 parameters for maximum signal-to-noise performance. *Concepts Magn Reson*  
833 2001;13:190–210.

- 834 49. Wu N, Peck TL, Webb AG, et al.  $^1\text{H}$ -NMR spectroscopy on the nanoliter scale for static  
835 and on-line measurements. *Anal Chem* 1994;66:3849–3857.
- 836 50. Webb AG. Microcoil nuclear magnetic resonance spectroscopy. *J Pharm Biomed Anal*  
837 2005;38:892–903.
- 838 51. Schroeder FC, Gronquist M. Extending the scope of NMR spectroscopy with microcoil  
839 probes. *Angew Chem Int Ed* 2006;45:7122–7131.
- 840 52. Kentgens AP, Bart J, van Bentum PJ, et al. High-resolution liquid- and solid-state  
841 nuclear magnetic resonance of nanoliter sample volumes using microcoil detectors. *J*  
842 *Chem Phys* 2008;128:052202.
- 843 53. Fratila RM, Velders AH. Small-volume nuclear magnetic resonance spectroscopy, *Annu*  
844 *Rev Anal Chem* 2011;4:227–249.
- 845 54. Webb AG. Radiofrequency microcoils for magnetic resonance imaging and  
846 spectroscopy. *J Magn Reson* 2013;229:55–66.
- 847 55. Badilita V, Meier RCh, Spengler N, et al. Microscale nuclear magnetic resonance : a tool  
848 for soft matter research. *Soft Matter* 2012;8:10583–10597
- 849 56. Korvink JG, MacKinnon N, Badilita V, Jouda M. "Small is beautiful" in NMR. *J Magn*  
850 *Reson* 2019;306:112–177.
- 851 57. Webb AG. Nuclear magnetic resonance coupled microseparations. *Magn Reson Chem*  
852 2005;43:688–696.
- 853 58. Lee, H, Yoon T–J, Figueiredo J–L, Swirski FK, Weissleder R. Rapid detection and  
854 profiling of cancer cells in fine-needle aspirates, *Proc Natl Acad Sci USA*  
855 2009;106:12459–12464.
- 856 59. Jeong S, Eskandari R, Park SM, et al. Real-time quantitative analysis of metabolic flux in  
857 live cells using a hyperpolarized micromagnetic resonance spectrometer. *Sci Adv*  
858 2017;3:e1700341.
- 859 60. Schlotterbeck G, Ross A, Hochstrasser R, et al. High-resolution capillary tube NMR. A  
860 miniaturized 5- $\mu\text{L}$  high-sensitivity TXI probe for mass-limited samples, off-line LC  
861 NMR, and HT NMR. *Anal Chem* 2002;74:4464–4471.
- 862 61. Edmond DT, Wormald MR. Theory of resonance in magnetically inhomogeneous  
863 specimens and some useful calculations. *J Magn Reson* 1988;77:223–232.
- 864 62. Yablonsky DA, Haacke EM. Theory of NMR signal behavior in magnetically  
865 inhomogeneous tissues: the static dephasing regime. *Magn Reson Med* 1994;32:749–763.
- 866 63. Webb AG, Grant SC. Signal-to-noise and magnetic susceptibility trade-offs in solenoidal  
867 microcoils for NMR. *J Magn Reson B* 1996;113:83–87.
- 868 64. Soffe N, Boyd J, Leonard M. The construction of a high-resolution 750 MHz probehead.  
869 *J Magn Reson A* 1995;116:117–121.
- 870 65. Zelaya FO, Crozier S, Dodd S, McKenna R, Doddrell DM. Measurement and  
871 compensation of field inhomogeneities caused by differences in magnetic-  
872 susceptibility. *J Magn Reson A* 1995;115:131–136.

- 873 66. Takeda K, Takasaki T, Takegoshi K. Susceptibility cancellation of a microcoil wound  
874 with a paramagnetic-liquid-filled copper capillary. *J Magn Reson* 2015;258:1–5.
- 875 67. De Zanche N, Barmet C, Nordmeyer-Massner JA, Pruessmann KP. NMR probes for  
876 measuring magnetic fields and field dynamics in MR systems. *Magn Reson Med*  
877 2008;60:176–186.
- 878 68. Kc R, Gowda YN, Djukovic D, et al. Susceptibility-matched plugs for microcoil NMR  
879 probes. *J Magn Reson* 2010;205:63–68.
- 880 69. Garroway AN. Magic-angle sample spinning of liquids. *J Magn Reson* 1982;49:168-171.
- 881 70. Barbara TM. Cylindrical demagnetization fields and microprobe design in high-  
882 resolution NMR. *J Magn Reson A* 1994;109:265–269.
- 883 71. Doty FD, Entzminger G, Yang AY. Magnetism in high-resolution NMR probe design. II:  
884 HR-MAS. *Concepts Magn Reson* 1998;10:239–260.
- 885 72. Lippens G, Bourdonneau M, Dhalluin C, et al. Study of compounds attached to solid  
886 supports using high resolution magic angle spinning NMR. *Current Org Chem*  
887 1999;3:147–169.
- 888 73. Feng J, Hu J, Burton SD, Hoyt DW. High resolution magic angle spinning <sup>1</sup>H NMR  
889 metabolic profiling of nanoliter biological tissues at high magnetic field. *Chinese J Magn*  
890 *Reson* 2013;30:1–11.
- 891 74. Wong A, Jiménez B, Li X, Holmes E, et al. Evaluation of high resolution magic-angle  
892 coil spinning NMR spectroscopy for metabolic profiling of nanoliter tissue biopsies.  
893 *Anal Chem* 2012;84:3843–3848.
- 894 75. Badilita V, Fassbender B, Kratt K, et al. Microfabricated inserts for magic angle coil  
895 spinning (MACS) wireless NMR spectroscopy. *PLoS ONE* 2012;7:1–8.
- 896 76. Wong A, Li X, Sakellariou D. Refined magic-angle coil spinning resonator for nanoliter  
897 NMR spectroscopy: enhanced spectral resolution. *Anal Chem* 2013;85:2021–2026.
- 898 77. Wong A, Li X, Molin L, et al.  $\mu$ HR-MAS spinning NMR spectroscopy for metabolic  
899 phenotyping of *Caenorhabditis elegans*. *Anal Chem* 2014;86:6064–6070.
- 900 78. Nishiyama Y, Endo Y, Nemoto T, et al. High-resolution NMR-based metabolic detection  
901 of microgram biopsies using a 1-mm HR $\mu$ MAS probe. *Analyst* 2015;140:8097–8100.
- 902 79. Lucas-Torres C, Huber G, Ichikawa A, et al. HR- $\mu$ MAS NMR-based metabolomics:  
903 localized metabolic profiling of a garlic clove with  $\mu$ g tissues. *Anal Chem*  
904 2018;90:13736–13743.
- 905 80. Adhikari SS, Zhao L, Dickmeis T, et al. Inductively coupled magic angle spinning  
906 microresonators benchmarked for high-resolution single embryo metabolomic profiling.  
907 *Analyst* 2019;144:7192–7199.
- 908 81. Lucas-Torres C, Roumes H, Bouchaud V, Bouzier-Sore A-K, Wong A. Metabolic NMR  
909 mapping with microgram tissue biopsy. *NMR Biomed* 2012;34:e4477.

- 910 82. Aguiar PM, Jacquinet J-F, Sakellariou D. Experimental and numerical examination of  
911 eddy (Foucault) currents in rotating micro-coils: generation of heat and its impact on  
912 sample temperatures. *J Magn Reson* 2009;200:6–14.
- 913 83. Piotto M, Elbayed K, Wieruszeshi J-M, Lippens G. Practical aspects of shimming a high  
914 resolution magic angle spinning probe. *J Magn Reson* 2005;173:84–89.
- 915 84. Wishart DS, Bigam CG, Yao J, et al. <sup>1</sup>H, <sup>13</sup>C and <sup>15</sup>N chemical shift referencing in  
916 biomolecular NMR. *J Biomol NMR* 1995;6:135–140.
- 917 85. Pontoizeau C, Mouchiroud L, Molin L, et al. Metabolomics analysis uncovers that  
918 dietary restriction buffers metabolic changes associated with aging in *Caenorhabditis*  
919 *elegans*. *J Proteome Res* 2014;13:2910–2919.
- 920 86. Wong A, Boutin C, Aguiar PM. <sup>1</sup>H high resolution magic-angle coil spinning (HR-  
921 MACS)  $\mu$ NMR metabolic profiling of whole *Saccharomyces cerevisiae* cells: A  
922 demonstrative study. *Front Chem* 2014;2:1–7.
- 923 87. Lehmann-Horn JA, Jacquinet J-F, Ginefri JC et al. Monolithic MACS micro resonators.  
924 *J Magn Reson* 2016;271:46–51.
- 925 88. Nishiyama M, Lucas-Torres C, Piao R, et al. Supplemental shimming for HR- $\mu$ MAS  
926 NMR spectroscopy. *Appl Magn Reson* 2019;50:1305–1313.
- 927 89. Sampol D, Ostrofet E, Jobin M-L, et al. Glucose and lactate metabolism in the awake  
928 and stimulated rat: a <sup>13</sup>C-NMR study. *Front Neuroenergetics* 2013;5:5.
- 929 90. Beckonert O, Coen M, Keun HC, et al. High-resolution magic-angle-spinning NMR  
930 spectroscopy for metabolic profiling of intact tissues. *Nat Protoc* 2010;5:1019–1032.
- 931 91. Beckonert O, Keun HC, Ebbels TMD, et al. Metabolic profiling, metabolomic and  
932 metabonomic procedures for NMR spectroscopy of urine, plasma, serum and tissue  
933 extracts. *Nat Protoc* 2007;2:2692–2703.
- 934 92. Kim HK, Choi YH, Verpoorte R. NMR-based metabolomic analysis of plants. *Nat*  
935 *Protoc* 2010;5:536–549.
- 936 93. Lucas-Torres C, Bernard T, Gaspard H, et al. General guidelines for sample preparation  
937 strategies in HR- $\mu$ MAS NMR-based metabolomics of microscopic specimens.  
938 *Metabolites* 2020;10:54.
- 939 94. Duong NT, Yamato M, Nakano M, et al. Capillary-inserted rotor design for HR $\mu$ MAS  
940 NMR-based metabolomics on mass-limited neurospheres. *Molecules* 2017;22:1289.
- 941 95. Allen NJ, Eroglu C. Cell biology of astrocyte-synapse interactions. *Neuron*  
942 2017;96:697–708.
- 943 96. Hamelin S, Stupar V, Mazière L, et al. In vivo  $\gamma$ -aminobutyric acid increase as a  
944 biomarker of the epileptogenic zone: an unbiased metabolomics approach. *Epilepsia*  
945 2021;62:163–175.
- 946 97. Kinross JM, Holmes E, Darzi AW, Nicholson, JK. Metabolic phenotyping for  
947 monitoring surgical patients. *Lancet* 2011;377:1817–1819.

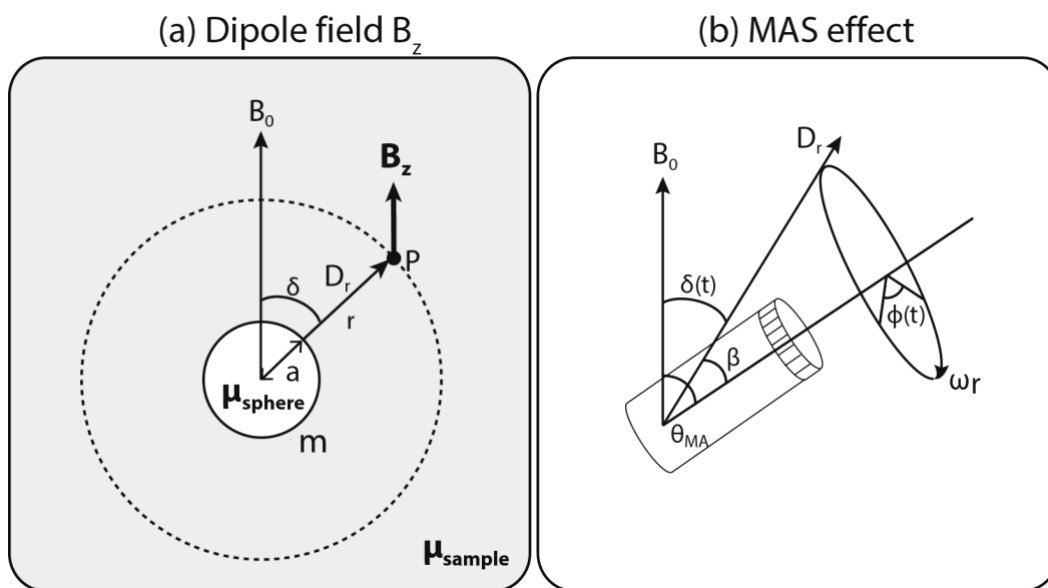
948 98. Feenstra AD, Alexander LE, Song Z, et al. Spatial mapping and profiling of metabolite  
949 distributions during germination. *Plant Physiol* 2017;174:2532–2548.

950

951

952

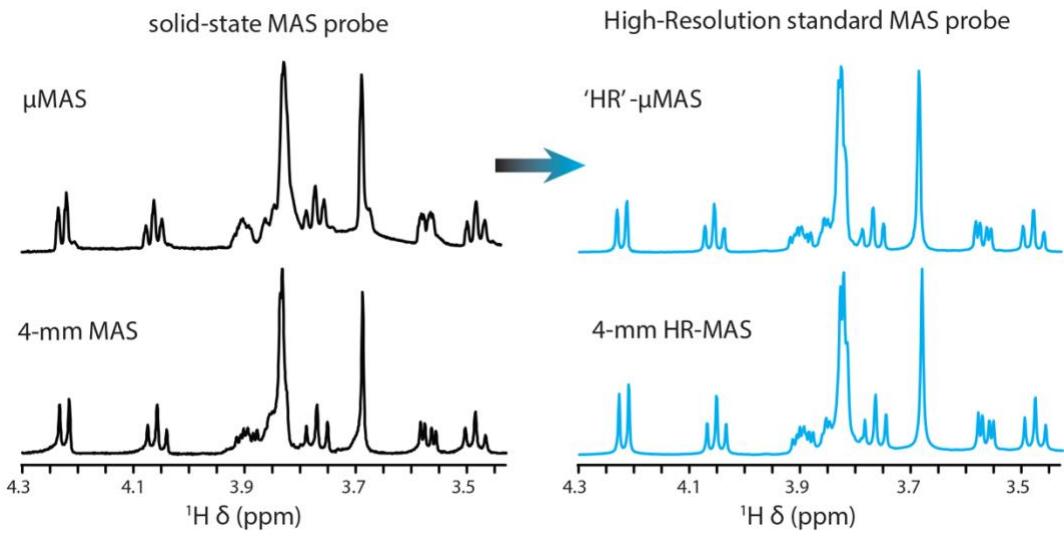
953



954  
 955  
 956  
 957  
 958  
 959  
 960

Figure 1

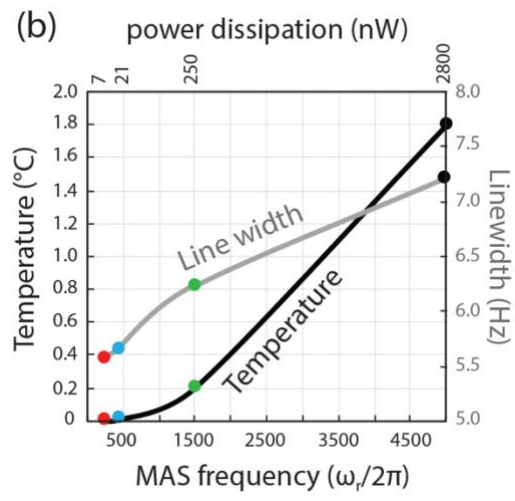
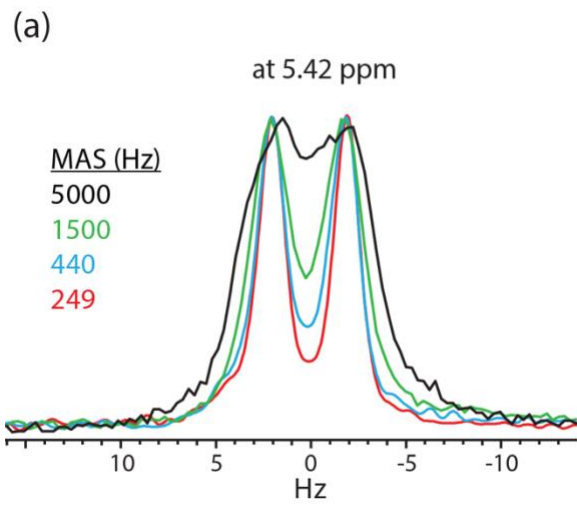
961  
962  
963



964  
965  
966  
967  
968  
969

Figure 2

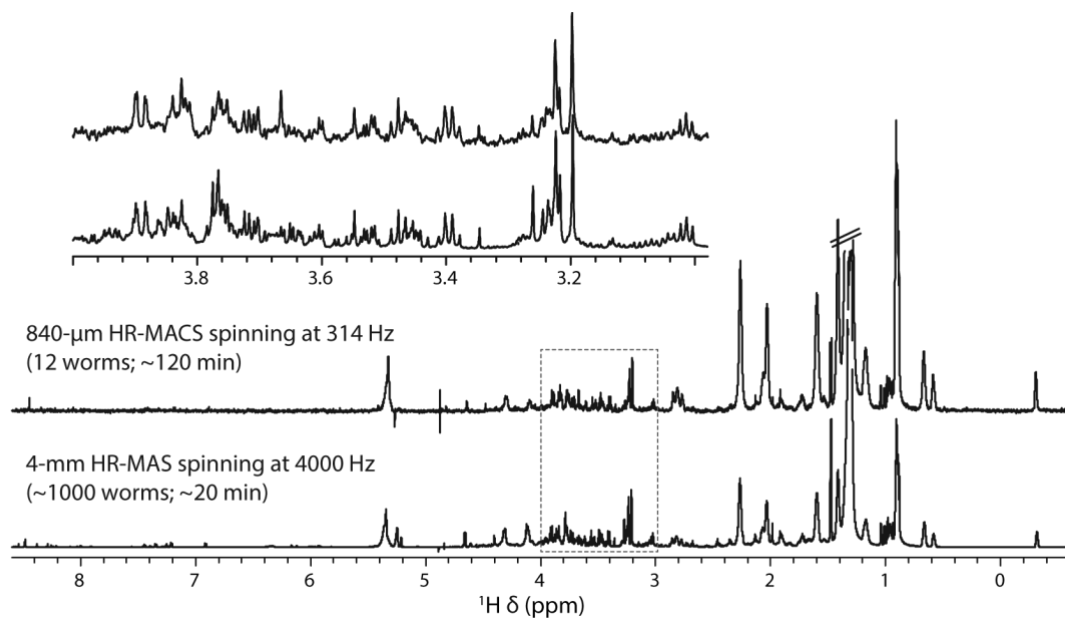
970  
971



972  
973  
974  
975  
976  
977

Figure 3

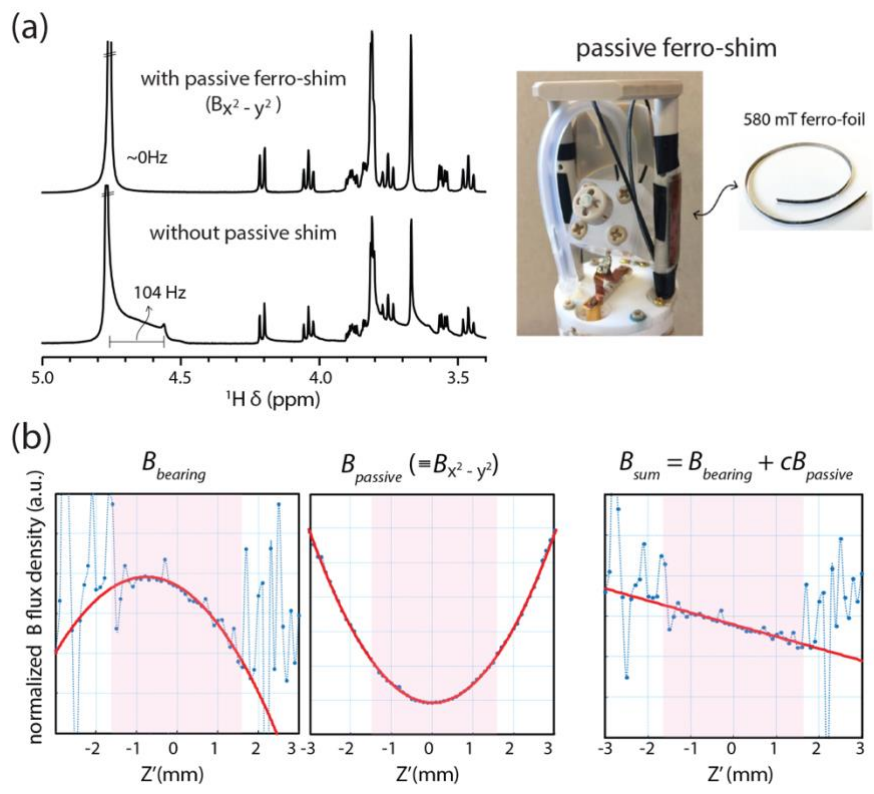
978  
979



980  
981  
982  
983  
984  
985

Figure 4

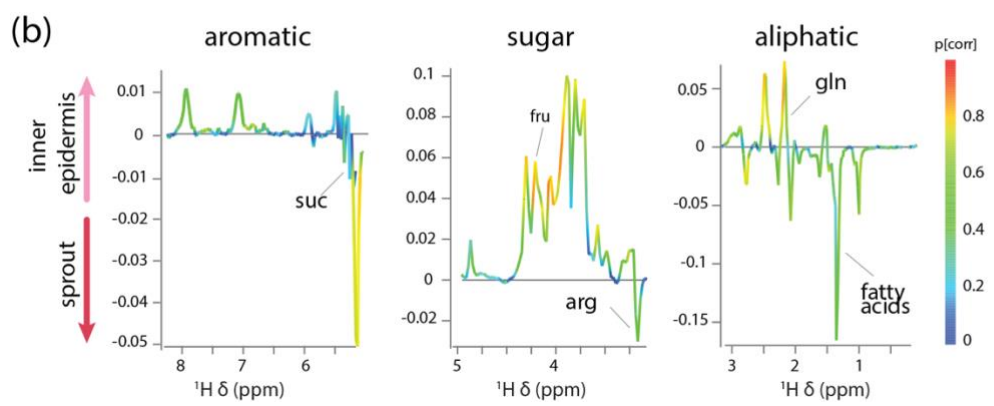
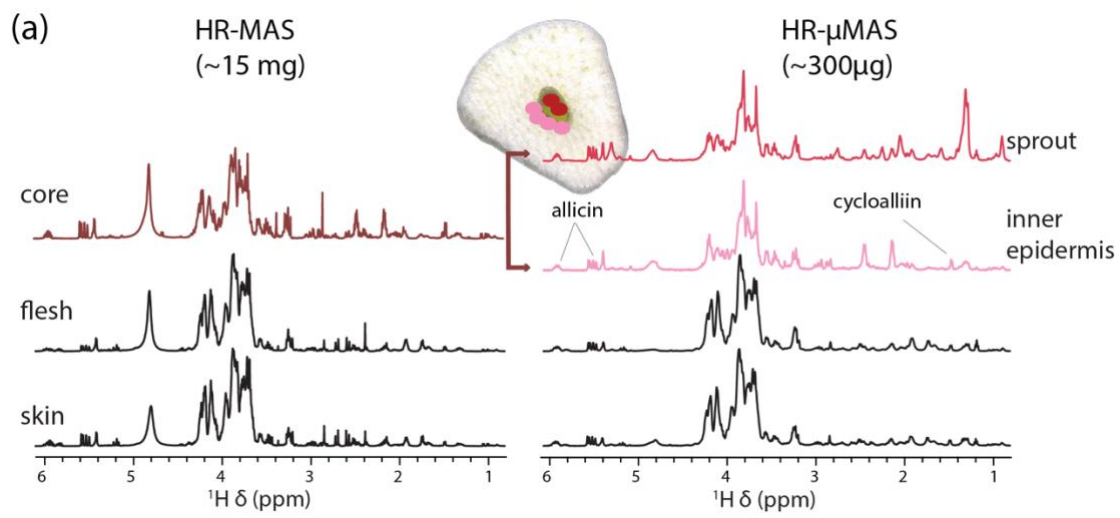
986  
987  
988



989  
990  
991  
992  
993  
994  
995  
996

Figure 5

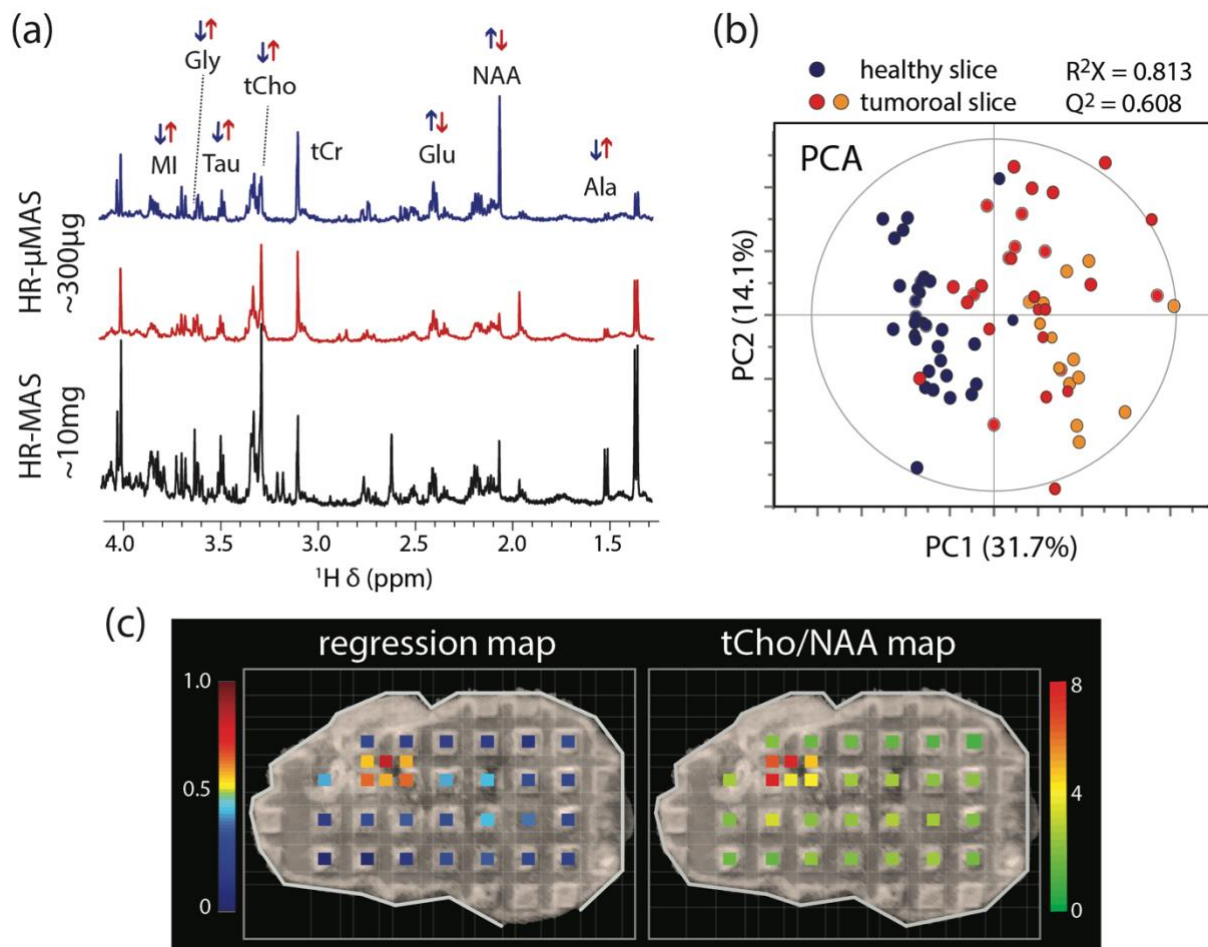
997  
998



999  
1000  
1001  
1002  
1003  
1004  
1005

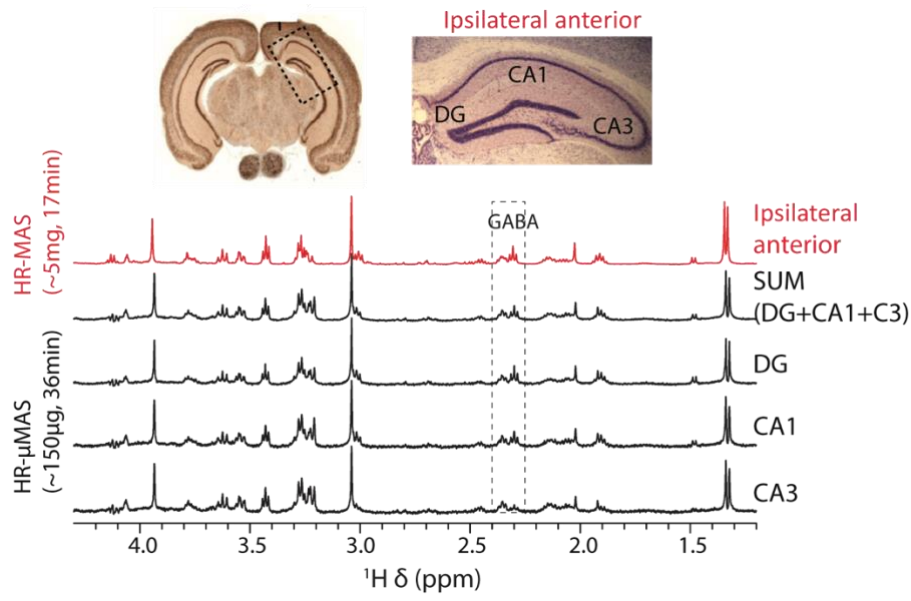
Figure 6

1006  
1007  
1008



1009  
1010  
1011  
1012  
1013  
1014

Figure 7



1015  
 1016  
 1017  
 1018  
 1019  
 1020  
 1021

Figure 8